

AD-A186 617

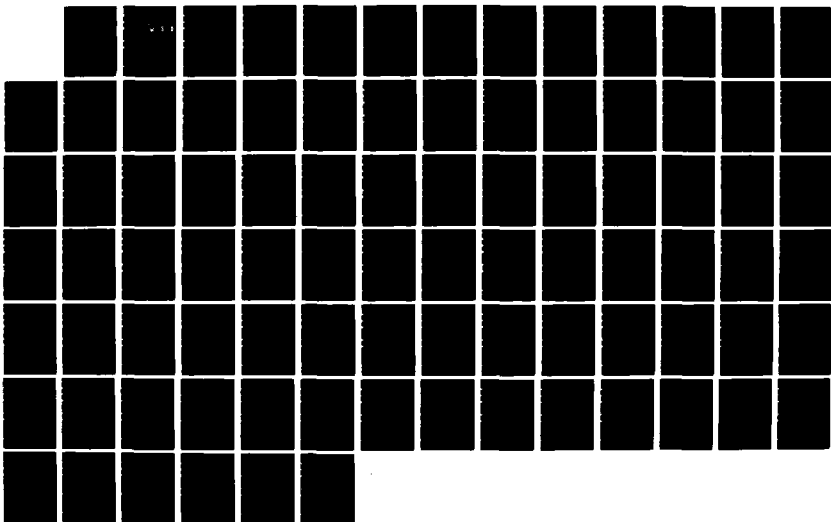
A STUDY OF FINITE DIFFERENCE AND FINITE ELEMENT
VERTICAL DISCRETIZATION SCHEMES FOR BAROCINIC
PREDICTION EQUATIONS(U) NAVAL POSTGRADUATE SCHOOL
MONTEREY CA 8 G SHAPIRO JUN 87

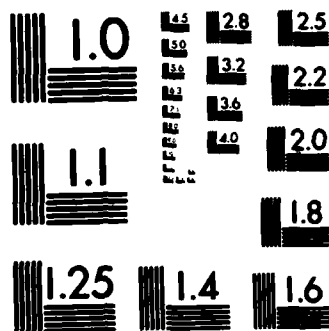
1/1

UNCLASSIFIED

F/G 4/2

NL





MICROCOPY RESOLUTION TEST CHART
NATIONAL BUREAU OF STANDARDS-1963-A

AD-A186 617

NAVAL POSTGRADUATE SCHOOL

Monterey, California

DTIC FILE COPY



DTIC
ELECTE
DEC 09 1987
S D
C.D.

THESIS

A STUDY OF FINITE DIFFERENCE AND FINITE
ELEMENT VERTICAL DISCRETIZATION SCHEMES
FOR BAROCLINIC PREDICTION EQUATIONS

by

Bruce G. Shapiro

June 1987

Thesis Advisor
Co-Advisor

Roger Terry Williams
Beny Neta

Approved for public release; distribution is unlimited.

87 1 004

REPORT DOCUMENTATION PAGE

1a REPORT SECURITY CLASSIFICATION UNCLASSIFIED			1b RESTRICTIVE MARKINGS		
2a SECURITY CLASSIFICATION AUTHORITY			3 DISTRIBUTION/AVAILABILITY OF REPORT Approved for public release; distribution is unlimited.		
2b DECLASSIFICATION/DOWNGRADING SCHEDULE			5 MONITORING ORGANIZATION REPORT NUMBER(S)		
4 PERFORMING ORGANIZATION REPORT NUMBER(S)			7a NAME OF MONITORING ORGANIZATION Naval Postgraduate School		
6a NAME OF PERFORMING ORGANIZATION Naval Postgraduate School		6b OFFICE SYMBOL (if applicable) 63	7b ADDRESS (City, State, and ZIP Code) Monterey, California 93943-5000		
8a NAME OF FUNDING/SPONSORING ORGANIZATION		8b OFFICE SYMBOL (if applicable)	9 PROCUREMENT INSTRUMENT IDENTIFICATION NUMBER		
8c ADDRESS (City, State, and ZIP Code)		10 SOURCE OF FUNDING NUMBERS			
		PROGRAM ELEMENT NO	PROJECT NO	TASK NO	WORK UNIT ACCESSION NO
11 TITLE (Include Security Classification) A STUDY OF FINITE DIFFERENCE AND FINITE ELEMENT VERTICAL DISCRETIZATION SCHEMES FOR BAROCLINIC PREDICTION EQUATIONS					
12 PERSONAL AUTHOR(S) Shapiro, Bruce G.					
13a TYPE OF REPORT Masters Thesis		13b TIME COVERED FROM TO		14 DATE OF REPORT (Year Month Day) 1987 June	
15 PAGE COUNT 87					
16 SUPPLEMENTARY NOTATION					
COSAT CODES			18 SUBJECT TERMS (Continue on reverse if necessary and identify by block number)		
FIELD	GROUP	SUB-GROUP	Numerical Weather Prediction, Finite Elements, Finite Differences, Baroclinic Instability		
9 ABSTRACT (Continue on reverse if necessary and identify by block number)					
The vertical discretization in a linearized baroclinic prediction model was analyzed by comparing various finite element and finite difference solutions following Jordan (1985). Modifications were made on Jordan's (1985) Galerkin finite element approximation for two staggered grids. Comparisons were made with the unmodified models (Jordan, 1985) and with finite difference approximations for the same two staggered grids. The models were run with four experiments. Most of the oscillations that occurred in the temperature profiles near the surface of the unmodified Galerkin finite element approximations disappeared following the modifications.					
19 DISTRIBUTION/AVAILABILITY OF ABSTRACT <input checked="" type="checkbox"/> UNCLASSIFIED UNLIMITED <input type="checkbox"/> SAME AS RPT <input type="checkbox"/> DTIC USERS			21 ABSTRACT SECURITY CLASSIFICATION unclassified		
22a NAME OF RESPONSIBLE INDIVIDUAL R. T. Williams/B. Neta			22b TELEPHONE (Include Area Code) 408-646-2296/2235		22c OFFICE SYMBOL 63Wu/53Nd

Approved for public release; distribution is unlimited.

A Study of Finite Difference and Finite Element
Vertical Discretization Schemes
for Baroclinic Prediction Equations

by


Bruce G. Shapiro
Second Lieutenant, United States Air Force
B.S., University of Utah, 1985

Submitted in partial fulfillment of the
requirements for the degrees of

MASTER OF SCIENCE IN METEOROLOGY
and
MASTER OF SCIENCE IN APPLIED MATHEMATICS

from the
NAVAL POSTGRADUATE SCHOOL
June 1987

Author:


Bruce G. Shapiro


Approved by:

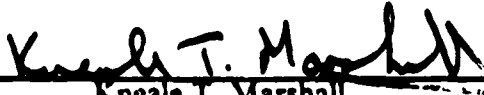

Roger Terry Williams, Thesis Advisor



Beny Neta, Co-Advisor


Robert J. Benard, Chairman,
Department of Meteorology


Gordon E. Schacher,
Dean of Science and Engineering


Kneale T. Marshall,
Dean of Information and Policy Sciences

ABSTRACT

The vertical discretization in a linearized baroclinic prediction model was analyzed by comparing various finite element and finite difference solutions following Jordan (1985). Modifications were made on Jordan's (1985) Galerkin finite element approximation for two staggered grids. Comparisons were made with the unmodified models (Jordan, 1985) and with finite difference approximations for the same two staggered grids. The models were run with four experiments. Most of the oscillations that occurred in the temperature profiles near the surface of the unmodified Galerkin finite element approximations disappeared following the modifications.

Accession For	
NTIS CR&I	<input checked="checked" type="checkbox"/>
DTIC TAB	<input type="checkbox"/>
Unannounced	<input type="checkbox"/>
Justification	
By	
Distribution	
Availability Codes	
Dist	Avail and/or Solicit
A-1	

TABLE OF CONTENTS

I.	INTRODUCTION	10
II.	MODEL DESCRIPTIONS	13
	A. MODEL FEATURES	13
	B. GOVERNING EQUATIONS	13
	C. TIME DIFFERENCING	19
	D. VERTICAL GRIDS	20
	E. FINITE DIFFERENCE MODELS	20
	F. FINITE ELEMENT MODELS	21
	1. FEM-A	21
	2. FEM-B	25
III.	EXPERIMENTS AND RESULTS	28
	A. ROSSBY WAVE EXPERIMENT	28
	1. Sixty-Layer Models	28
	2. Six-Layer Models	29
	B. MOUNTAIN TOPOGRAPHY EXPERIMENT	30
	1. Sixty-Layer Models	30
	2. Six-Layer Models	31
	C. DIABATIC HEATING EXPERIMENT	31
	1. Sixty-Layer Models	31
	2. Six and Twelve-Layer Models	32
	D. BAROCLINIC INSTABILITY EXPERIMENT	33
	1. Sixty-Layer Models	33
	2. Six-Layer Models	34
IV.	CONCLUSIONS	68
	APPENDIX A: FINITE DIFFERENCE APPROXIMATIONS	70

APPENDIX B:	GALERKIN FORM OF FEM-A PROGNOSTIC EQUATIONS	71
APPENDIX C:	BASIS FUNCTION EQUATIONS FOR FEM-A	74
APPENDIX D:	GALERKIN FORM OF FEM-B PROGNOSTIC EQUATIONS	76
APPENDIX E:	FORCED VERTICAL VELOCITY	78
APPENDIX F:	DIABATIC HEATING TERMS	80
	LIST OF REFERENCES	82
	INITIAL DISTRIBUTION LIST	84

LIST OF FIGURES

1.1	Two vertical grids.	12
2.1	Basis functions for grids A and B.	21
3.1	Sixty-layer Rossby wave experiment at 96 hours. Temperature amplitude profiles (top) and temperature phase profiles (bottom) are compared.	35
3.2	Sixty-layer Rossby wave experiment at 96 hours. Divergence amplitude profiles (top) and divergence phase profiles (bottom) are compared.	36
3.3	Sixty-layer Rossby wave experiment at 96 hours from Jordan (1985). <i>Temperature amplitude profiles are compared for models FEM-A</i> <i>(top) and FEM-B (bottom) and FDM-C, which represents the</i> <i>consensus profile.</i>	37
3.4	Six-layer Rossby wave experiment at 96 hours. Temperature amplitude profiles are compared for the six-layer and sixty-layer FDM-A (top) and FDM-B (bottom) models.	38
3.5	Six-layer Rossby wave experiment at 96 hours. Temperature amplitude profiles are compared for the six-layer and sixty-layer FEM-A (top) and FEM-B (bottom) models.	39
3.6	Six-layer Rossby wave experiment at 96 hours. Divergence amplitude profiles are compared for the six-layer and sixty-layer FDM-A (top) and FDM-B (bottom) models.	40
3.7	Six-layer Rossby wave experiment at 96 hours. Divergence amplitude profiles are compared for the six-layer and sixty-layer FEM-A (top) and FEM-B (bottom) models.	41
3.8	Sixty-layer mountain topography experiment at 96 hours. <i>Temperature amplitude profiles (top) and temperature phase profiles</i> <i>(bottom) are compared.</i>	42
3.9	Sixty-layer mountain topography experiment at 96 hours. Divergence amplitude profiles (top) and divergence phase profiles (bottom) are compared.	43
3.10	Sixty-layer mountain topography experiment at 96 hours from Jordan (1985). <i>Temp. (top) and divergence (bottom) amplitude profiles are</i> <i>compared for models FEM-A and FDM-C, which represents the</i> <i>consensus profile.</i>	44

3.11	Sixty-layer mountain topography experiment at 96 hours from Jordan (1985). Temperature amplitude (top) and phase (bottom) profiles are compared for models FEM-B and FDM-C, which represents the consensus profile.	45
3.12	Six-layer mountain topography experiment at 96 hours. Temperature amplitude profiles (top) and divergence amplitude profiles (bottom) are compared.	46
3.13	Six-layer mountain topography experiment at 96 hours. Temperature amplitude profiles are compared for the six-layer and sixty-layer FEM-A (top) and FEM-B (bottom) models.	47
3.14	Six-layer mountain topography experiment at 96 hours. Divergence amplitude profiles are compared for the six-layer and sixty-layer FEM-A (top) and FEM-B (bottom) models.	48
3.15	Six-layer mountain topography experiment at 96 hours. Divergence amplitude profiles are compared for the six-layer and sixty-layer FDM-A model.	49
3.16	Sixty-layer diabatic heating experiment at 96 hours. Temperature amplitude profiles (top) and temperature phase profiles (bottom) are compared.	50
3.17	Sixty-layer diabatic heating experiment at 12 hours from Jordan (1985). Temperature amplitude profiles are compared for models FEM-A (top) and FEM-B (bottom) and FDM-C, which represents the consensus profile.	51
3.18	Sixty-layer diabatic heating experiment at 96 hours. Divergence amplitude profiles (top) and divergence phase profiles (bottom) are compared.	52
3.19	Sixty-layer diabatic heating experiment at 12 hours from Jordan (1985). Divergence amplitude (top) and phase (bottom) profiles are compared for models FEM-A and FDM-C, which represents the consensus profile.	53
3.20	Sixty-layer diabatic heating experiment at 12 hours. divergence phase profiles are compared for models FEM-A and FDM-A, which represents the consensus profile.	54
3.21	Six-layer diabatic heating experiment at 96 hours. Temperature amplitude profiles (top) and temperature phase profiles (bottom) are compared.	55
3.22	Six-layer diabatic heating experiment at 96 hours. Divergence amplitude profiles (top) and divergence phase profiles (bottom) are compared.	56
3.23	Twelve-layer diabatic heating experiment at 96 hours. Temperature amplitude profiles (top) and temperature phase profiles (bottom) are compared.	57

3.24	Twelve-layer diabatic heating experiment at 96 hours. Divergence amplitude profiles (top) and divergence phase profiles (bottom) are compared.	58
3.25	Twelve-layer diabatic heating experiment at 96 hours. Divergence amplitude profiles are compared for the twelve-layer and sixty-layer FDM-A (top) and FEM-A (bottom) models.	59
3.26	Twelve-layer diabatic heating experiment at 96 hours. Divergence amplitude profiles are compared for models FDM-A, FDM-B, FEM-A, FEM-B and sixty-layer FEM-B, which represents the consensus profile.	60
3.27	Sixty-layer baroclinic instability experiment at 96 hours. Temperature amplitude profiles (top) and temperature phase profiles (bottom) are compared.	61
3.28	Sixty-layer baroclinic instability experiment at 96 hours. Divergence amplitude profiles (top) and divergence phase profiles (bottom) are compared.	62
3.29	Sixty-layer baroclinic instability experiment at 96 hours. Temperature phase profiles are compared on a closer scale. Compare Fig. 3.27(bottom).	63
3.30	Six-layer baroclinic instability experiment at 96 hours. Temperature amplitude profiles (top) and temperature phase profiles (bottom) are compared.	64
3.31	Six-layer baroclinic instability experiment at 96 hours. Divergence amplitude profiles (top) and divergence phase profiles (bottom) are compared.	65
3.32	Six-layer baroclinic instability experiment at 96 hours. Temperature amplitude profiles are compared for models FDM-A, FDM-B, FEM-A, and sixty-layer FDM-A, which represents the consensus profile.	66
3.33	Six-layer baroclinic instability experiment at 96 hours. Temperature amplitude profiles are compared for the six-layer and sixty-layer FEM-B model.	67

ACKNOWLEDGEMENTS

Thanks go to Mary Jordan who wrote the numerical models used in this study. I would like to thank Dr. Beny Neta for his help in the numerical model modification, and Dr. R. Terry Williams for his help in the interpretation of the results of the experiments. My wife, Mischell deserves the greatest thanks for her support, help and her understanding during the many hours that I was with the computer and not with her.

I. INTRODUCTION

Most numerical weather prediction models use finite differences to accomplish the vertical discretization even though they use finite difference, finite element, or spectral, horizontal discretizations. The only exceptions are the Canadian regional and hemispheric models (Staniforth and Daley, 1977 and 1979), which use finite elements in the vertical. The successful numerical prediction of synoptic evolutions requires a proper representation of the vertical variation of the predictive fields. Since smaller scale features such as fronts (Hoskins and Bretherton, 1972 and Williams, 1967) and the large scale planetary waves (Gall, 1976) are forced by energetic synoptic-scale features, it follows that all predictive scales of motion may be sensitive to the vertical discretization used in the numerical models.

Most of the finite difference vertical discretizations use a staggered arrangement of variables. It has been demonstrated that staggering of variables in the horizontal (Winninghoff, 1968; Arakawa and Lamb, 1977 and Schoenstadt, 1980) improves geostrophic adjustment and the response to small scale forcing. Most quasi-geostrophic models (Charney and Phillips, 1953) use vertical staggering where the vertical motion and the temperature are carried between the levels which carry horizontal velocity and pressure. This arrangement will be referred to as grid B. Lorenz (1960) introduced a different grid for the balance equations which was designed to conserve energy. This arrangement places only the vertical velocity between the levels which carry the other variables (horizontal velocity, pressure and temperature) and will be referred to as grid A. Tokioka (1978) analyzed a number of vertical grids with linearized equations and found that grid A has a computational mode in the temperature field. Arakawa (1980) compared baroclinic instability for grids A and B in the linearized quasi-geostrophic equations. He found a false short wave instability for grid A which did not occur with grid B. This problem is related to the computational mode in the temperature field. Another difficulty with grid B is that the matrix which must be inverted to find the temperature from the pressure is singular. This is especially important for initialization. Many operational primitive equation models use grid A for energy conservation.

The use of finite elements for the vertical discretization can be expected to give a more accurate representation of vertical variations. The finite element method is a

special case of the Galerkin procedure which represents the dependent variables with a weighted sum of basis functions that have a prescribed spatial structure. The finite element method employs basis functions which are zero except in a limited region where they are low-order polynomials. This method was developed in engineering statics (see e.g., Zienkiewicz, 1977) and it has been more recently applied to fluid dynamics and hydrology (see Gray and Pinder, 1976). The finite element method has been successfully applied to meteorological prediction with the shallow water equations by Cullen (1973), Hinsman (1975) and Staniforth and Mitchell (1977, 1978). Cullen (1973), Neta et al (1986), and Neta and Williams (1986) demonstrated that finite element formulations with piecewise linear basis functions are more accurate than second order finite differences.

Jordan (1985) compared six linear, baroclinic, vorticity-divergence equation models using three grid schemes, grid A, grid B and an unstaggered grid. A perturbation was found in the temperature fields of the Rossby wave experiment and the mountain topography experiment in the finite element models using grids A and B (Fig. 1.1).

The purpose of this study is to see if the perturbations noted in the Jordan study could be fixed. A baroclinic instability experiment is made with a comparison of finite element and finite difference models for grids A and B. The finite element models for grids A and B are modified at the boundaries and the finite difference models for grids A and B are left as they were except for the necessary modifications to run the baroclinic instability experiment. The results of the modified models are compared with the results of the unmodified models from Jordan (1985) for the Rossby wave experiment, the mountain topography experiment and the diabatic heating experiment. The experiments are described in Chapter III.

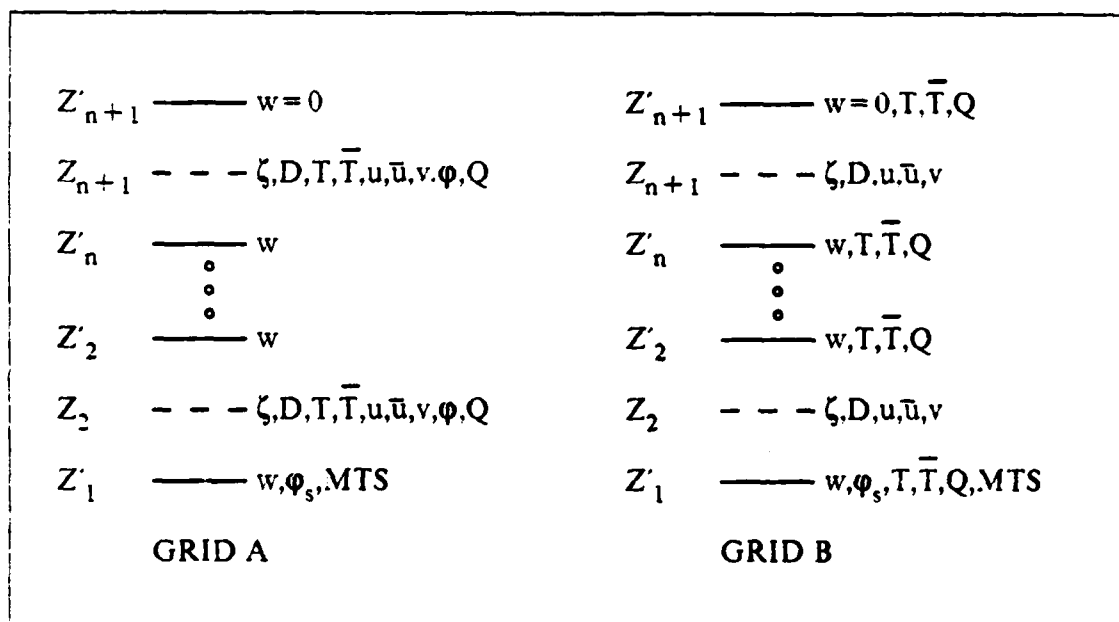


Fig. 1.1 Two vertical grids.

II. MODEL DESCRIPTIONS

A. MODEL FEATURES

Jordan (1985) developed six numerical models with several features to make easy modifications for a wide range of experiments. A menu is added to each of the models to make the transition between four experiments simple. The user is able to prescribe heating, mountain topography, velocity perturbation, or baroclinic experiments and the model will make the prescribed changes in the variables governing these cases. Another menu is added so that the user can prescribe the amount of printout desired from each run. The models are written in modular structure using FORTRAN '77. There is parallel construction between models. The subroutines used in one model are very similar to those used in the other models. The models run quickly on an IBM-3033 mainframe; for example, a 96-hour forecast for a 12 layer finite element model uses less than five seconds of computer processing time.

B. GOVERNING EQUATIONS

Each model approximates the same set of governing equations. The vorticity equation (2.1), the divergence equation (2.2), the surface geopotential equation (2.3), and the first law of thermodynamics (2.4) are the prognostic equations for the forecast variables vorticity, divergence, surface geopotential and potential temperature. The surface geopotential equation is the lower boundary condition on the vertical velocity. The vertical coordinate $Z = -\ln(p/p_0)$ is used, but the non-Boussinesq terms involving e^{-Z} are replaced by one. The prognostic equations in the coordinates x , y , Z , and t are:

$$\frac{d\zeta}{dt} + (\zeta + f)D + \beta v + \frac{\partial w}{\partial x} \frac{\partial v}{\partial Z} - \frac{\partial w}{\partial y} \frac{\partial u}{\partial Z} = 0, \quad (2.1)$$

$$\begin{aligned} \frac{dD}{dt} + \frac{\partial u}{\partial x} \frac{\partial u}{\partial x} + \frac{\partial v}{\partial y} \frac{\partial v}{\partial y} + 2 \frac{\partial u}{\partial y} \frac{\partial v}{\partial x} + \frac{\partial w}{\partial x} \frac{\partial u}{\partial Z} \\ + \frac{\partial w}{\partial y} \frac{\partial v}{\partial Z} + \beta u - f\zeta + \nabla^2 \phi = 0, \end{aligned} \quad (2.2)$$

$$\frac{d\phi_s}{dt} = MTS, \quad (2.3)$$

$$\frac{dT}{dt} = Q. \quad (2.4)$$

In these equations:

ζ is the vertical component of vorticity, $\zeta = \partial v / \partial x - \partial u / \partial y$,

D is the horizontal divergence, $D = \partial u / \partial x + \partial v / \partial y$,

ϕ is the geopotential, $\phi = gZ$,

ϕ_s is the surface geopotential,

T is the potential temperature,

u is the x-component of velocity,

v is the y-component of velocity,

w is the vertical velocity,

Q is the diabatic heating per unit time per unit mass,

MTS is the forced vertical velocity due to flow over mountain topography, which will

be discussed in Chapter III,

f is the Coriolis parameter,

β is df/dy ,

$$\frac{d(\)}{dt} = \frac{\partial(\)}{\partial t} + u \frac{\partial(\)}{\partial x} + v \frac{\partial(\)}{\partial y} + w \frac{\partial(\)}{\partial Z}, \text{ and}$$

∇^2 is the horizontal Laplacian operator.

The prognostic equations are linearized by expanding the variables into their mean and perturbation states, as in Jordan (1985). The resulting linearized forecast equations are:

$$\frac{\partial \zeta'}{\partial t} = -f D' - \bar{u} \frac{\partial \zeta'}{\partial x} - \beta v', \quad (2.5)$$

$$\frac{\partial D'}{\partial t} = f \zeta' - \bar{u} \frac{\partial D'}{\partial x} - \beta u' - \frac{\partial w}{\partial x} \frac{d\bar{u}}{dZ} - \frac{\partial^2 \phi'}{\partial x^2}, \quad (2.6)$$

$$\frac{\partial \phi_s'}{\partial t} = -\bar{u} \frac{\partial \phi_s'}{\partial x} - v' \frac{\partial \bar{\phi}_s}{\partial y} - R \bar{T} w' + M T S', \quad (2.7)$$

$$\frac{\partial T'}{\partial t} = -\bar{u} \frac{\partial T'}{\partial x} - v' \frac{\partial \bar{T}}{\partial y} - w' \frac{\partial \bar{T}}{\partial Z} + Q'. \quad (2.8)$$

where R is the gas constant for air, $(')$ denotes perturbation quantities and $(-)$ denotes mean quantities. The use of \bar{X} in the text will be used to denote mean quantities of a variable X .

The diagnostic variables, u' , v' , w' and ζ' , are calculated from the forecast variables using the definitions of divergence, vorticity, the hydrostatic equation and the continuity equation. The relationships are given in equations 2.9 through 2.12.

$$\frac{\partial u'}{\partial x} = D'. \quad (2.9)$$

$$\frac{\partial v'}{\partial x} = \zeta'. \quad (2.10)$$

$$\frac{\partial \phi'}{\partial x} = R T'. \quad (2.11)$$

$$D' + \frac{\partial w'}{\partial Z} = 0. \quad (2.12)$$

The use of primes to denote perturbation quantities will be discontinued. All quantities used in the remainder of the paper will be perturbation quantities unless otherwise noted.

The mean state is assumed to be in hydrostatic and geostrophic balance. The term $\partial \bar{T} / \partial y$ in the first law of thermodynamics can be evaluated by taking $\partial / \partial y$ of the hydrostatic equation and substituting for $\partial \bar{\phi} / \partial y$ from the geostrophic relation, $\partial \bar{\phi} / \partial y = -f \bar{u}$. Thus,

$$\frac{\partial \bar{T}}{\partial y} = -\frac{f}{R} \frac{\partial \bar{u}}{\partial Z} \quad (2.13)$$

Geostrophic balance of the mean state at the surface implies

$$\frac{\partial \bar{\phi}_s}{\partial y} = -f \bar{u}_{sfc} \quad (2.14)$$

The expressions (2.13) and (2.14) are substituted into equations (2.8) and (2.7), respectively.

A singlewave spectral representation is used in the x-direction, with wave number $\mu = 2\pi/L$, where L is the wavelength in the x-direction. The perturbation quantities have the form:

$$\zeta(x,Z,t) = A_1(Z,t) \cos \mu x + A_2(Z,t) \sin \mu x, \quad (2.15)$$

$$D(x,Z,t) = D_1(Z,t) \cos \mu x + D_2(Z,t) \sin \mu x, \quad (2.16)$$

$$T(x,Z,t) = T_1(Z,t) \cos \mu x + T_2(Z,t) \sin \mu x, \quad (2.17)$$

$$\phi_s(x,Z,t) = S_1(Z,t) \cos \mu x + S_2(Z,t) \sin \mu x, \quad (2.18)$$

$$u(x,Z,t) = U_1(Z,t) \cos \mu x + U_2(Z,t) \sin \mu x, \quad (2.19)$$

$$v(x,Z,t) = V_1(Z,t) \cos \mu x + V_2(Z,t) \sin \mu x, \quad (2.20)$$

$$w(x,Z,t) = W_1(Z,t) \cos \mu x + W_2(Z,t) \sin \mu x , \quad (2.21)$$

$$\varphi(x,Z,t) = H_1(Z,t) \cos \mu x + H_2(Z,t) \sin \mu x . \quad (2.22)$$

$$Q(x,Z,t) = Q_1(Z,t) \cos \mu x + Q_2(Z,t) \sin \mu x , \quad (2.23)$$

$$MTS(x,Z,t) = MTS_1(Z,t) \cos \mu x + MTS_2(Z,t) \sin \mu x . \quad (2.24)$$

The relations (2.15) through (2.24) are substituted into equations (2.5) through (2.12). The prognostic and diagnostic equations are separated into equations for the cosine and sine terms. The resultant prognostic equations are:

$$\frac{\partial A_1}{\partial t} = -f D_1 - \bar{u} \mu A_2 - \beta V_1 , \quad (2.25)$$

$$\frac{\partial A_2}{\partial t} = -f D_2 + \bar{u} \mu A_1 - \beta V_2 , \quad (2.26)$$

$$\frac{\partial D_1}{\partial t} = f A_1 - \bar{u} \mu D_2 - \beta U_1 - \mu \frac{d\bar{u}}{dZ} W_2 + \mu^2 H_1 , \quad (2.27)$$

$$\frac{\partial D_2}{\partial t} = f A_2 + \bar{u} \mu D_1 - \beta U_2 + \mu \frac{d\bar{u}}{dZ} W_1 + \mu^2 H_2 , \quad (2.28)$$

$$\frac{\partial T_1}{\partial t} = -\bar{u} \mu T_2 + \frac{f}{R} \frac{d\bar{u}}{dZ} V_1 - \frac{\partial \bar{T}}{\partial Z} W_1 + Q_1 , \quad (2.29)$$

$$\frac{\partial T_2}{\partial t} = \bar{u}\mu T_1 + \frac{f}{R} \frac{d\bar{u}}{dZ} V_2 - \frac{\partial \bar{T}}{\partial Z} W_2 + Q_2 . \quad (2.30)$$

$$\frac{\partial S_1}{\partial t} = -\bar{u}\mu S_2 + f\bar{u}V_1 - R\bar{T}W_1 + MTS_1 . \quad (2.31)$$

$$\frac{\partial S_2}{\partial t} = \bar{u}\mu S_1 + f\bar{u}V_2 - R\bar{T}W_2 + MTS_2 . \quad (2.32)$$

The resultant diagnostic equations for u and v are:

$$U_1 = -\frac{D_2}{\mu} , \quad (2.33)$$

$$U_2 = \frac{D_1}{\mu} , \quad (2.34)$$

$$V_1 = -\frac{A_2}{\mu} , \quad (2.35)$$

$$V_2 = \frac{A_1}{\mu} . \quad (2.36)$$

Geopotential values above the surface are obtained by integrating the hydrostatic equation from the surface ($Z = Z_0$) to height Z :

$$H_1 = R \int_{Z_0}^Z T_1(Z,t) dZ + S_1 . \quad (2.37)$$

$$H_2 = R \int_{Z_0}^Z T_2(Z,t) dZ + S_2 . \quad (2.38)$$

The vertical velocity is calculated by integrating the continuity equation from the top of the atmosphere ($Z = Z_T$) down to height Z . The upper boundary condition, $w = 0$

at $Z = Z_T$, is used. This boundary condition is not exact, but some form of it is used in most numerical models. The diagnostic equations for the vertical velocity are:

$$W_1 = \int_{Z_0}^Z D_1(Z,t) dZ, \quad (2.39)$$

$$W_2 = \int_{Z_0}^Z D_2(Z,t) dZ. \quad (2.40)$$

Equations (2.25) through (2.40) are the prognostic and diagnostic equations that govern all four numerical models. Using the given basic state and the one-wave spectral perturbation quantities, the governing equations reduce to functions of Z and t . The models are effectively one-dimensional.

To display the results of each model, the sine and cosine amplitudes of each variable are combined to determine the amplitude and phase of a single cosine wave in the x -direction. A typical variable has the form:

$$Y(x,Z,t) = A(Z,t) \cos(\mu x - \delta). \quad (2.41)$$

where the amplitude is $A(Z,t)$ and the phase is $\delta(Z,t)$. The amplitude and phase are calculated at each level for all variables.

C. TIME DIFFERENCING

Two forward time steps are taken to start each model and then leapfrog time differencing is used. The leapfrog scheme is employed because of its ease to code. A Robert filter is used to reduce the amplitude of the computational mode generated by the leapfrog time differencing. The filter is discussed by Haltiner and Williams (1980). For a prognostic variable F , calculate \bar{F}_{n-1} , the average value of F at time step $(n-1)\Delta t$, using equation (2.42),

$$\bar{F}_{n-1} = F_{n-1} + \gamma(F_n - 2F_{n-1} + \bar{F}_{n-2}), \quad (2.42)$$

where γ is a weighting function. Using the unaveraged values at time step $n\Delta t$, compute the tendency $(\partial F / \partial t)_n$ from its predictive equation. The predicted value at time step $(n+1)\Delta t$ is then calculated using equation (2.43),

$$F_{n+1} = \bar{F}_{n-1} + 2\Delta t \left(\frac{\partial F}{\partial t} \right)_n. \quad (2.43)$$

In all the experiments, $\gamma = 0.05$ is used. The time step for each experiment is calculated in the model by requiring, for computational stability,

$$v\Delta t = \frac{1}{2}, \quad (2.44)$$

where $v = \mu c$, and c is the typical phase speed of an external gravity wave.

D. VERTICAL GRIDS

Each of the models uses one of two vertical grids. The two ways used to distribute the variables over discrete levels are depicted in Fig. 1.1. The staggered levels are represented by the dashed lines in Fig. 1.1. Notice that the heights at which the variables are defined change between the two grids. The notation used in this paper to denote the staggered and unstaggered levels is consistent with the conventions used in the coded models. The height of the unstaggered levels is denoted as Z' . The height of the staggered levels is denoted as Z . In the models, both Z'_1 and Z_1 are defined to be the surface of the earth. It is assumed that the staggered level Z_i is exactly in the middle of the layer between Z'_{i-1} and Z'_i . This distinction is important because the models can have layers with unequal depth. Thus, the height of the staggered levels is defined relative to the height of the unstaggered levels.

A finite difference model is written for each of the grid structures. The models are denoted as FDM-A and FDM-B. Similarly, finite element models using the two grids are indicated by FEM-A and FEM-B.

E. FINITE DIFFERENCE MODELS

The only differences in the equations between the two FDM models are the approximations of terms involving \overline{du}/dZ and $\partial \overline{T}/\partial Z$ in the prognostic equations and the approximations of the integral in the diagnostic geopotential equation. Centered difference approximations are used, except at the boundaries where one-sided differences are employed. The finite difference approximations used in the prognostic equations are listed in Appendix A.

F. FINITE ELEMENT MODELS

1. FEM-A

The FEM-A model defines vertical velocity (w) at the unstaggered levels in terms of the basis functions $\psi_j(Z)$. The other variables are defined at the staggered levels in terms of the basis functions $\phi_j(Z)$. The expansion for a typical term is

$$A_1(Z,t) = \sum_{j=1}^{n+1} A_1^j(t) \phi_j(Z). \quad (2.45)$$

The basis functions for this model are depicted in Fig. 2.1. The basis functions $\psi(Z)$ are defined for the unstaggered levels (solid lines at height Z') and the basis functions $\phi(Z)$ are defined for the staggered levels (dashed lines at height Z).

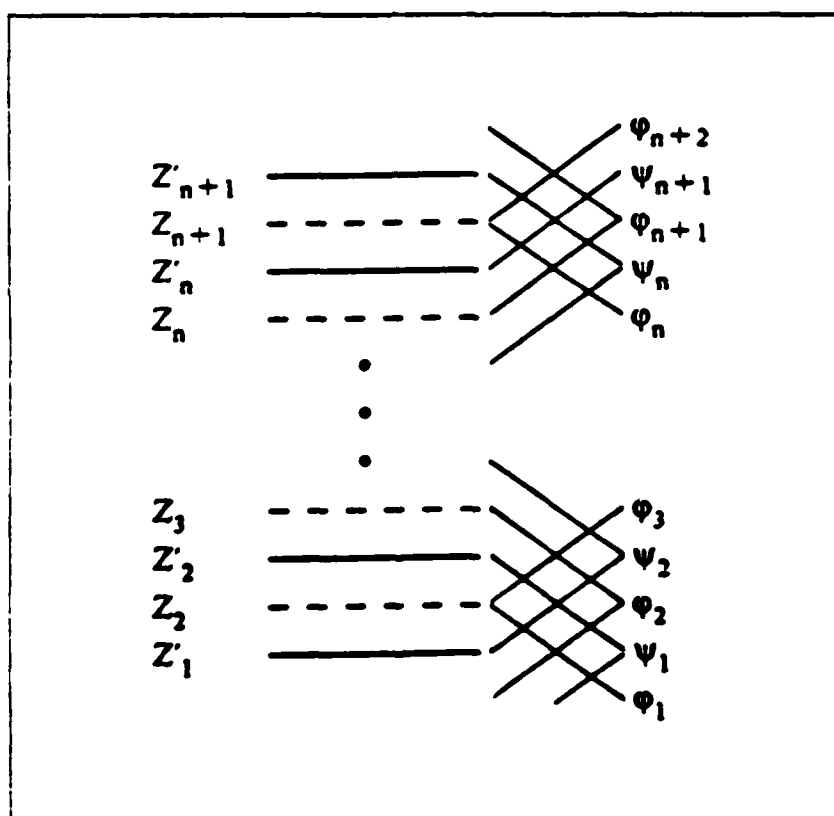


Fig. 2.1 Basis functions for grids A and B.

The finite element approximations for the vorticity, divergence and thermodynamic equations are derived by substituting the expansion for each dependent variable into equations (2.25) through (2.30). Each equation is multiplied by $\phi_i(Z)$ and integrated with respect to Z from the bottom to the top of the atmosphere. Each term in the equations is the finite sum of separate integrals. Only the integrals of overlapping basis functions are nonzero. The resultant equations, listed in Appendix B, are matrix equations. For an N -layer model, the vectors, $A_1, A_2, D_1, D_2, H_1, H_2, Q_1, Q_2, T_1, T_2, U_1, U_2, V_1$, and V_2 , contain $n+2$ components. The vectors W_1 , and W_2 contain $n+1$ components. The matrices M, K , and Φ , defined below, are $(n+2) \times (n+2)$ matrices. The matrix P , defined below, is an $(n+1) \times (n+2)$ matrix.

The mass matrix M for this model is defined by

$$M_{ij} = \int_{Z_0}^{Z_T} \phi_j(Z) \phi_i(Z) dZ \quad \text{for } |i-j| \leq 1. \quad (2.46)$$

The matrix K is defined for terms multiplied by \bar{u} ,

$$K_{ij}(\bar{u}) = \sum_{k=i-1}^{i+1} \bar{u}^k \int_{Z_0}^{Z_T} \phi_j(Z) \phi_k(Z) \phi_i(Z) dZ \quad \text{for } |i-j| \leq 1. \quad (2.47)$$

The matrix P is defined for terms multiplied by $\frac{d\bar{u}}{dZ} W$, or by $\frac{d\bar{T}}{dZ} W$,

$$P_{ij}(\bar{x}) = \sum_{k=i-1}^{i+1} \bar{x}^k \int_{Z_0}^{Z_T} \frac{d\phi_k}{dZ} \phi_j(Z) \phi_i(Z) dZ \quad \text{for } |i-j| \leq 1. \quad (2.48)$$

where $x = u$, or T .

The matrix Φ is defined for terms multiplied by $\frac{d\bar{u}}{dZ} V$,

$$\Phi_{ij}(\bar{u}) = \sum_{k=i-1}^{i+1} \bar{u}^k \int_{Z_0}^{Z_T} \frac{d\phi_k}{dZ} \phi_j(Z) \phi_i(Z) dZ \quad \text{for } |i-j| \leq 1. \quad (2.49)$$

The staggered basis functions present two general problems for evaluating the elements of the four matrices. First, for an n -layer model, portions of basis functions $\phi_1(Z)$ and $\phi_{n+2}(Z)$ are defined in the model atmosphere but the physical meaning of contributions from those terms is unclear. The contributions are included in the first two rows and the last row of each matrix. Second, only portions of basis functions $\phi_2(Z)$ and $\phi_{n+1}(Z)$ are defined in the model atmosphere. To describe the incomplete sides of both basis functions an assumption must be made about the value of ϕ_2 at the surface and ϕ_{n+1} at the top of the atmosphere.

Assumptions are made and procedures are developed on an attempt to resolve these problems. In this model the mean state variables, \bar{u} and \bar{T} , are defined only at the n staggered levels. However, \bar{u} and \bar{T} values defined at the nodal points of $\phi_1(Z)$ and $\phi_{n+2}(Z)$ are important in the Galerkin formulation of the $\bar{u} dZ$ and $\partial \bar{T} / \partial Z$ terms. In these experiments, the values of \bar{u} and \bar{T} are defined at the surface and top of the atmosphere. Jordan (1985) did not define them at the nodal points of $\phi_1(Z)$ and $\phi_{n+2}(Z)$. One of the major modifications of these experiments is to define \bar{u} and \bar{T} at the nodal points of $\phi_1(Z)$ and $\phi_{n+2}(Z)$. For constant shear with height, \bar{u} and \bar{T} are defined at the boundaries such that the shear in the two half layers at the boundaries is the same as the shear in the other layers. To evaluate the staggered basis functions defined in the layers between the surface and Z_2 , and Z_{n+1} and the top of the atmosphere, it is assumed that the value at the boundaries of those basis functions is one-half. Thus, three-fourths of the basis functions $\phi_2(Z)$ and $\phi_{n+2}(Z)$ are defined in the model atmosphere.

The equations for the general elements of the four matrices are evaluated by substituting into equations (2.46) through (2.49) the formulas for $\phi_{i+1}(Z)$, $\phi_i(Z)$, $\phi_{i-1}(Z)$, $\psi_{i+1}(Z)$, $\psi_i(Z)$, $\psi_{i-1}(Z)$, and $\psi_{i-2}(Z)$, in terms of the local coordinate $\xi_i = Z - Z_i$. The equations for these basis functions defined for the levels 1, 2, i , and $n+1$, are listed in Appendix C. The matrices were evaluated by integrating numerically using 2 point Gaussian Quadratures.

The vorticity, divergence and thermodynamic equations, written in matrix and vector form, are:

$$\mathbf{M} \frac{d\mathbf{A}_1}{dt} = \mathbf{M}(-f\mathbf{D}_1 - \beta\mathbf{V}_1) - \mu\mathbf{K}(\bar{u})\mathbf{A}_2, \quad (2.50)$$

$$\mathbf{M} \frac{d\mathbf{A}_2}{dt} = \mathbf{M}(-f\mathbf{D}_2 - \beta\mathbf{V}_2) + \mu\mathbf{K}(\bar{u})\mathbf{A}_1, \quad (2.51)$$

$$\mathbf{M} \frac{d\mathbf{D}_1}{dt} = \mathbf{M}(f\mathbf{A}_1 - \beta\mathbf{U}_1 + \mu^2\mathbf{H}_1) - \mu\mathbf{K}(\bar{u})\mathbf{D}_2 - \mu\mathbf{P}(\bar{u})\mathbf{W}_1, \quad (2.52)$$

$$\mathbf{M} \frac{d\mathbf{D}_2}{dt} = \mathbf{M}(f\mathbf{A}_2 - \beta\mathbf{U}_2 + \mu^2\mathbf{H}_2) + \mu\mathbf{K}(\bar{u})\mathbf{D}_1 - \mu\mathbf{P}(\bar{u})\mathbf{W}_2, \quad (2.53)$$

$$\mathbf{M} \frac{d\mathbf{T}_1}{dt} = -\mathbf{K}(\bar{u})\mathbf{T}_2 + \frac{f}{R}\Phi(\bar{u})\mathbf{V}_1 - \mathbf{P}(\bar{T})\mathbf{W}_1 + \mathbf{M}\mathbf{Q}_1, \quad (2.54)$$

$$\mathbf{M} \frac{d\mathbf{T}_2}{dt} = \mathbf{K}(\bar{u})\mathbf{T}_1 + \frac{f}{R}\Phi(\bar{u})\mathbf{V}_2 - \mathbf{P}(\bar{T})\mathbf{W}_2 + \mathbf{M}\mathbf{Q}_2. \quad (2.55)$$

Equations (2.50) through (2.55) are simplified by multiplying each equation by \mathbf{M}^{-1} and applying the Robert filter. Actually one should not compute the inverse of \mathbf{M} . Instead at $t=0$ one should obtain the LU factorization of \mathbf{M} . Thus at each time step one only needs to forward and back solve a triangular system. The matrices $\mathbf{M}^{-1}\mathbf{K}$, $\mathbf{M}^{-1}\mathbf{P}$, and $\mathbf{M}^{-1}\Phi$ are constants. They are constructed in the initialization subroutine and stored for use in the forecast subroutine. The matrices are multiplied by the appropriate vectors with values for time level $n\Delta t$. The resultant forecast equations are vector equations and the forecast value for the i -th vertical level is the sum of values in the i -th location of each vector equation. The prognostic equations for the vorticity, divergence and potential temperature vectors are:

$$\mathbf{A}_{1(n+1)} = \mathbf{A}_{1(n-1)} + 2\Delta t(-f\mathbf{D}_1 - \beta\mathbf{V}_1 - \mu\mathbf{M}^{-1}\mathbf{K}(\bar{u})\mathbf{A}_2)_{(n)}, \quad (2.56)$$

$$\mathbf{A}_{2(n+1)} = \mathbf{A}_{2(n-1)} + 2\Delta t(-f\mathbf{D}_2 - \beta\mathbf{V}_2 + \mu\mathbf{M}^{-1}\mathbf{K}(\bar{u})\mathbf{A}_1)_{(n)}, \quad (2.57)$$

$$D_{1(n+1)} = D_{1(n-1)} + 2\Delta t (f A_1 - \beta U_1 + \mu^2 H_1 - \mu M^{-1} K(\bar{u}) D_2 - \mu M^{-1} P(\bar{u}) W_2)_{(n)}, \quad (2.58)$$

$$D_{2(n+1)} = D_{2(n-1)} + 2\Delta t (f A_2 - \beta U_2 + \mu^2 H_2 - \mu M^{-1} K(\bar{u}) D_1 + \mu M^{-1} P(\bar{u}) W_1)_{(n)}, \quad (2.59)$$

$$T_{1(n+1)} = T_{1(n-1)} + 2\Delta t (M^{-1} K(\bar{u}) T_2 + \frac{f}{R} M^{-1} \Phi(\bar{u}) V_1 - M^{-1} P(\bar{T}) W_1 + Q_1)_{(n)}, \quad (2.60)$$

$$T_{2(n+1)} = T_{2(n-1)} + 2\Delta t (-M^{-1} K(\bar{u}) T_1 + \frac{f}{R} M^{-1} \Phi(\bar{u}) V_2 - M^{-1} P(\bar{T}) W_2 + Q_2)_{(n)}, \quad (2.61)$$

where the subscripts $(n+1)$, (n) and $(n-1)$ refer to the values of the vectors at time step $(n+1)\Delta t$, $n\Delta t$ and $(n-1)\Delta t$, respectively.

The surface geopotential and the diagnostic variables are calculated using the corresponding equations in model FDM-A (see Appendix A).

2. FEM-B

The FEM-B model defines vertical velocity, potential temperature, mean state potential temperature and diabatic heating at the unstaggered levels in terms of the basis functions $\psi_j(Z)$. The other variables are defined at the staggered levels in terms of the basis functions $\phi_j(Z)$. The basis functions are the same as defined for the FEM-A model, shown in Fig. 2.1.

The finite element approximations for the vorticity, divergence and thermodynamic equations are derived by substituting the expansion for each dependent variable into equations (2.25) through (2.30). The vorticity and divergence equations are multiplied by $\phi_i(Z)$ and integrated with respect to Z from the bottom to the top of the atmosphere. The resultant Galerkin formulation of the vorticity and divergence equations are the same as those derived for model FEM-A. The matrices in those equations, M , K , and P , are given by equations (2.46) through (2.48) as defined for FEM-A. The thermodynamic equations are multiplied by $\psi_i(Z)$ because potential temperature is defined at the unstaggered levels. As before, the equations are integrated

through the depth of the atmosphere. The resultant equations are listed in Appendix D. Four additional matrices are defined for the two thermodynamic equations. The mass matrix Π is

$$\Pi_{ij} = \int_{Z_0}^{Z_T} \psi_j(Z) \psi_i(Z) dZ \quad \text{for } |i-j| \leq 1. \quad (2.62)$$

The matrix Γ is defined for terms multiplied by \bar{u} ,

$$\Gamma_{ij}(\bar{u}) = \sum_{k=i-1}^{i+1} \bar{u}^k \int_{Z_0}^{Z_T} \psi_j(Z) \phi_k(Z) \psi_i(Z) dZ \quad \text{for } |i-j| \leq 1. \quad (2.63)$$

Terms multiplied by $\frac{d\bar{u}}{dZ} V$, give rise to the transpose of the matrix \mathbf{P} , defined by (2.48).

The matrix Ψ is defined for terms multiplied by $\frac{d\bar{T}}{dZ} W$,

$$\Psi_{ij}(\bar{T}) = \sum_{k=i-1}^{i+1} \bar{T}^k \int_{Z_0}^{Z_T} \frac{d\psi_k}{dZ} \psi_j(Z) \psi_i(Z) dZ \quad \text{for } |i-j| \leq 1. \quad (2.65)$$

As discussed in the FEM-A model description, the staggered finite elements present problems for evaluating the elements of the matrices. In this model \bar{u} is defined at the surface, the top of the atmosphere, and at the n staggered levels. The mean state temperature, \bar{T} , is defined at the unstaggered levels so special definitions for it are not needed. Jordan (1985) did not include the contributions from the perturbation quantities defined at the nodal points of $\phi_1(Z)$ and $\phi_{n+2}(Z)$. They were included in this model as part of the modifications of this experiment. The staggered basis functions, $\phi_i(Z)$, are evaluated at the boundaries using the assumptions discussed in the previous section.

The elements of matrices Π , Γ , and Ψ are evaluated by substituting formulas for $\phi_{i+2}(Z)$, $\phi_{i+1}(Z)$, $\phi_i(Z)$, $\phi_{i-1}(Z)$, $\psi_{i+1}(Z)$, $\psi_i(Z)$, and $\psi_{i-1}(Z)$, defined in

terms of the local coordinate $\xi = Z - Z_i$, into equations (2.62), (2.63), and (2.65). Formulas for these basis functions are listed in Appendix C. As in FEM-A the matrices are evaluated by integrating numerically using 2 point Gaussian Quadratures.

The forecast matrix equations for vorticity, divergence and temperature are simplified in a manner similar to the method described for model FEM-A. The final form of the vorticity and divergence vector equations are the same as for model FEM-A, equations (2.56) through (2.59). The thermodynamic vector equations are:

$$\begin{aligned} T_{1(n+1)} = & T_{1(n-1)} \\ & + 2\Delta t \left(+\mu \Pi^{-1} \Gamma(\bar{u}) T_2 + \frac{f}{R} \Pi^{-1} P^T(\bar{u}) V_1 - \Pi^{-1} \Psi(\bar{T}) W_1 + Q_1 \right)_{(n)}. \end{aligned} \quad (2.66)$$

$$\begin{aligned} T_{2(n+1)} = & T_{2(n-1)} \\ & + 2\Delta t \left(-\mu \Pi^{-1} \Gamma(\bar{u}) T_1 + \frac{f}{R} \Pi^{-1} P^T(\bar{u}) V_2 - \Pi^{-1} \Psi(\bar{T}) W_2 + Q_2 \right)_{(n)}. \end{aligned} \quad (2.67)$$

In this model the vectors, $A_1, A_2, D_1, D_2, H_1, H_2, U_1, U_2, V_1$, and V_2 , contain $n+2$ components. The vectors Q_1, Q_2, T_1, T_2, W_1 , and W_2 contain $n+1$ components. The matrices Π, Γ , and Ψ are $(n+1) \times (n+1)$ matrices and the matrix P^T is an $(n+2) \times (n+1)$ matrix. The surface geopotential and the diagnostic variables are calculated using the corresponding equations in model FDM-B.

III. EXPERIMENTS AND RESULTS

Four experiments are performed with each model; an initial perturbation in the meridional flow, flow over mountain topography, flow with a diabatic heat source and baroclinic flow with vertical shear in the u bar field. The first two and the last experiments are performed with six- and then sixty-layer models. The heating experiment is repeated with six-, twelve- and sixty-layer models. The analytic solution of each experiment has not been derived. For each experiment, the sixty-layer model results are intercompared to determine if the models are converging to the same solution. The standard of comparison for each six-layer model is its corresponding sixty-layer solution. Temperature and divergence profiles are examined in each experiment.

Several parameters are defined identically in each experiment. The vertical coordinate, Z is defined between zero and one (1000–368mb) and the vertical levels are equally spaced. The x -wavelength is 4,000 kilometers. The time step is 17.7 minutes. The Coriolis parameter is defined at 45 degrees latitude. The mean state potential temperature increases with height from its surface value of 310.0 degrees K (Kelvin).

A. ROSSBY WAVE EXPERIMENT

Rossby waves are generated in each model using an initial perturbation, $v' = 5.0$ meters second (m/s), in the cosine term of the meridional flow. All other perturbations are initially zero. There is no diabatic heat source and no mountain topography. There is no vertical shear in the u bar field and $u_{\text{bar}} = 10.0$ m/s. The latitudinal variation of the Coriolis parameter, β , is defined at 45 degrees latitude. The forecast experiments are terminated at 96 hours.

1. Sixty-Layer Models

The sixty-layer FDM-A, FDM-B, and FEM-B models converge to the same temperature and divergence solutions (Figs. 3.1–3.2). All figures will be found at the end of the chapter. Note that the staggered models FDM-A and FEM-A are defined as zero at their lowest level because this level is below the bottom of the atmosphere. It should also be noted that the phase of each variable is defined between zero and 360 degrees. There is a discontinuity in the phase profile if the phase passes through zero degrees. The height at which the temperature phase discontinuity in model FDM-A

occurs differs from the other two models because temperature is defined at the staggered levels in FDM-A. The three models represent the same physical solution, which is called the consensus solution.

The FEM-A temperature amplitude is slightly smaller than the consensus amplitude, 2% at height $Z = 0.10$, and an amplitude oscillation is present in the lowest three layers of the atmosphere. In the results of Jordan (1985) (Fig. 3.3(top)), the FEM-A solution had a 32% difference from the consensus solution at height $Z = 0.10$ and a much more jagged profile in the lowest three layers of the atmosphere. Jordan (1985) felt that this jagged profile may be caused by the terms in the matrices which represent contributions from the basis functions near the lower boundary of the model. The FEM-A model is modified near the boundary to correct this problem. The FEM-A temperature phase is within 0.1 degree of the consensus. It is high enough to pass through zero one level above the consensus. The shape of the FEM-A divergence amplitude is consistent with that of the consensus amplitude, however it is slightly lower at the bottom and slightly higher at the top of the atmosphere. The consensus divergence phase is nearly constant with height and the divergence phase profile for model FEM-A is almost identical with the consensus profile.

In the results of Jordan (1985) (Fig. 3.3(bottom)) the FEM-B solution had a 5% difference from the consensus solution and a major oscillation in the lower layers of the atmosphere. The FEM-B model is modified near the boundary to correct this problem and is now part of the consensus solution (Figs. 3.1–3.2)

2. Six-Layer Models

The comparison of six- and sixty-layer profiles for variables defined at staggered levels may be initially misleading. The first staggered level in a six-layer model occurs at $Z = 0.0833$. The lowest staggered level in a sixty-layer model is defined at $Z = 0.0083$, which may be mistaken for the surface in the graphs. When the values of a six-layer model coincide with a sixty-layer profile, the models are considered to represent the same physical solution, even though the six-layer model has a smaller vertical domain for staggered variables.

The temperature amplitude profiles of the six-layer models are very similar to their corresponding sixty-layer results (Figs. 3.4–3.5). The previously discussed problems in the lowest three layers of model FEM-A are still slightly evident in the lowest three layers of the six-layer profile (Fig. 3.5(top)). The six-layer profile of the FEM-A model is nevertheless a very good approximation of the consensus profile.

The six-layer divergence amplitude profiles for the grid A models approximate their sixty-layer counterparts in a similar manner (Figs. 3.6(top)—3.7(top)). And the six-layer divergence amplitude profiles for the grid B models approximate their sixty-layer counterparts in a similar manner also (Figs. 3.6(bottom)—3.7(bottom)). The grid B models more closely approximate the sixty-layer consensus profile in the lower half of the atmosphere and the grid A models more closely approximate the sixty-layer consensus profile in the upper half of the atmosphere. The six-layer profile of the FEM-A model is the closest of the four in their approximation of their sixty-layer counterparts and the sixty-layer consensus profile (Fig. 3.7(top)).

B. MOUNTAIN TOPOGRAPHY EXPERIMENT

The forced vertical velocity term, MTS, in the surface geopotential forecast equation (2.3) is non-zero in this experiment. It represents the contribution to surface geopotential from air flowing over mountain topography which varies sinusoidally in the x-direction and has no variation in the y-direction. The mountain ridge-to-valley height difference is 1,500 meters. To reduce the trauma for the model, the mountains are gradually "built" to their full height over a period of 36 hours. Thus, the forced vertical velocity increases in the first 36 hours of the forecast period and is constant for the remainder of the 96-hour forecast period. The equations used to define the forced vertical velocity are included in Appendix E. There is no vertical shear in the \bar{u} field and $\bar{u} = 10.0$ m/s. β and all other initial perturbations are zero in this experiment.

1. Sixty-Layer Models

The FDM-A, FDM-B, and FEM-B models converge to the same physical solution for temperature and divergence (Figs. 3.8 and 3.9).

The FEM-A temperature amplitude is again slightly smaller than the consensus amplitude (2%) and a small oscillation is again present in the lowest three layers of the atmosphere. The FEM-A temperature phase and divergence phase solutions are exactly the same as the consensus solutions. The FEM-A divergence amplitude is only very slightly lower than the consensus amplitude at the bottom of the atmosphere (0.5%) and is indistinguishable from the consensus profile by $Z = 0.20$. Jordan (1985) found that the temperature amplitude of the unmodified FEM-A model was 30% higher than the consensus near the bottom of the atmosphere (Fig. 3.10(top)) and that the divergence amplitude of the unmodified FEM-A model was higher at the bottom of the atmosphere and lower at the top of the atmosphere than the consensus (Fig. 3.10(bottom)).

Jordan (1985) again found a jagged temperature amplitude profile in the unmodified FEM-B model in the lowest two layers of the atmosphere (Fig. 3.11(top)) and the temperature amplitude was 5% more than the consensus near the surface. The unmodified FEM-B temperature phase profile was jagged in the lowest three layers and top two layers of the atmosphere while the rest of the profile was within one degree of the consensus (Fig. 3.11(bottom)). The modified FEM-B profiles are now part of the consensus in every case for this experiment (Figs. 3.8 and 3.9).

2. Six-Layer Models

The temperature amplitude profiles of the six-layer models FDM-A, FDM-B, and FEM-B are identical with each other and also with the consensus solution (Figs. 3.12(top) and 3.13(bottom)). The slight oscillation in the lowest three layers of the FEM-A model is still slightly evident in the six-layer model (Fig. 3.13(top)), however the six-layer model profile is still very close to the consensus profile (Fig. 3.12(top)).

The six-layer divergence amplitude profiles are very close to the sixty-layer consensus (Figs. 3.14 and 3.12(bottom)). Both of the six-layer finite element model divergence amplitude profiles are closer to the sixty-layer consensus divergence amplitude profile than the FDM-A profile (Figs. 3.14 and 3.15)

C. DIABATIC HEATING EXPERIMENT

A diabatic heat source is defined in the layer between $Z = 0.40$ and $Z = 0.60$ (670–549mb). The rate of heating is constant in time and varies in x and Z ,

$$Q(x,Z,t) = \text{HEATING} \cos^2\left(\frac{Z - Z_M}{Z_U - Z_L} \pi\right) \cos(\mu x) . \quad (3.1)$$

where HEATING is 5.0 K/day, Z_M is the midpoint of the heated layer, and Z_L and Z_U are the lower and upper boundaries of the heated layer, respectively. The diabatic heating vectors, Q_1 and Q_2 , are defined in the initialization subroutine and stored for use in the forecast subroutine. There is no vertical shear in the u bar field and u bar = 10.0 m s. β and all other initial perturbations are zero in this experiment. The forecast length is 96 hours, however, a 12-hour forecast is made for comparison with Jordan (1985).

1. Sixty-Layer Models

For the diabatic heating function defined in equation (3.1), the maximum heating occurs at $Z = 0.50$, the midpoint of the heated layer. The models defined

using grid B define temperature and the heating functions at this point. The grid A models do not have temperature and diabatic heating defined at this point so the maximum rate of heating in these models is slightly less than in the other models, and the maximum heating occurs throughout one layer rather than occurring at one point. The heating rate at each level is listed in Appendix F for the six-, twelve- and sixty-layer models.

The sixty-layer profiles for the four models are quite similar, the differences occur mainly because the models are responding to different forcing. The temperature amplitude profiles for the B grids come to a sharp point at $Z = 0.50$ and the grid A models have a square-nosed profile around this point (Fig. 3.16(top)). The previously identified temperature amplitude oscillations in the lowest layers of models FEM-A and FEM-B were not evident in the unmodified models (Jordan, 1985) (Fig. 3.17) and are not evident in any of the modified models (Figs. 3.16(top)). This is because the heating is defined far enough away from the boundaries so that the previous problems with the basis functions at the bottom and the top of the atmosphere do not show up here. Note that there is a jagged profile at the bottom and top of the heated layer in the twelve hour forecasts because they are not steady state yet. In summary, the sixty-layer temperature profiles of all four models represent the same physical response to the diabatic heating.

The shape of the divergence amplitude profile is not symmetric around $Z = 0.50$ because divergence is not defined exactly at the midpoint of the heated layer in either of grids A or B (Fig. 3.18(top)). The divergence amplitude is identical outside the heated layer for all models except FEM-A which was also true at 12 hours with the unmodified models (Jordan, 1985), (Fig. 3.19(top)). The divergence phase profiles are virtually identical for all models in this experiment. Jordan (1985) found that the divergence phase for the unmodified FEM-A model at 12 hours was slightly different from the consensus outside the heated layer (Fig. 3.19(bottom)). The modified FEM-A model profile at 12 and 96 hours is exactly the same as the consensus profile (Figs. 3.20 and 3.18(bottom)).

2. Six and Twelve-Layer Models

The difference between grids is more evident in this experiment than in the other experiments. Each model is run with both six and twelve layers and the results are compared with the sixty-layer consensus of the four models.

The six-layer grid A model temperature and divergence amplitude fields barely respond to the diabatic heating (Figs. 3.21(top) and 3.22(top)). The grid A models are only about 6% of the amplitude of the grid B models. Comparing the maximum diabatic heating terms for the two grids, in Appendix F, it is found that the maximum heating in the grid A models is only about 6% of the maximum heating in the grid B models. This is because heating is defined to be greatest at the midpoint of the heated layer and decrease as you get away from the midpoint. Grid B defines heating at the maximum, or midpoint and grid A defines heating at points equidistant from the midpoint. As the number of layers gets smaller the distance between the midpoint and the first layer in grid A which is used to define heating increases, thus decreasing the value of the heating that goes into the layer.

The grid A models have a stronger response to heating with twelve layers than with six layers because with twelve layers heating is defined closer to the maximum at the midpoint of the heated layer (Figs. 3.21–3.22). The six- and twelve-layer models converge to the sixty-layer profile equally well for the finite element models as for the finite difference model for grid B (Figs. 3.23 and 3.24). For grid A the twelve-layer divergence amplitude is closer to the corresponding 60 layer profile for the finite element than for the finite difference model (Fig. 3.25) but the finite difference twelve-layer profile is closer to the consensus (Fig. 3.26).

D. BAROCLINIC INSTABILITY EXPERIMENT

Vertical shear in the \bar{u} field is defined in this experiment. The wind profile is a linear function of Z , with $\bar{u} = (\text{STRGTH}) Z$, where STRGTH defines the strength of the wind at the top of the atmosphere in m/s. In this experiment STRGTH is defined as 40 m/s. Waves are generated in each model using an initial perturbation, $v' = 5.0$ m/s in the cosine term of the meridional flow. β and all other perturbations are initially zero. There is no diabatic heat source and no mountain topography. The forecast experiments are terminated at 96 hours.

1. Sixty-Layer Models

The sixty-layer FDM-A, and FDM-B models converge to the same solution for the temperature amplitude, temperature phase, divergence amplitude and divergence phase (Figs. 3.27 and 3.28).

The FEM-A model shows a slightly higher temperature amplitude than the consensus profile but the shape is the same as the consensus profile. The same problem is evident for the divergence amplitude profile but the magnitude of the error

is smaller. The FEM-A model shows no sign of the oscillation that is evident near the surface in the Rossby wave experiment and the mountain topography experiment. This may be because the \bar{u} field is almost zero near the bottom of the atmosphere where Z is small which cancels out the problem with the basis function that may be causing the oscillation in the other experiments. The FEM-A model profile is almost identical with the consensus for temperature phase and identical with the consensus profile for divergence phase.

The FEM-B model profile shows a lower temperature amplitude than the consensus profile and the shape is the same except for a small oscillation that occurs in the lowest three layers of the atmosphere. This oscillation is not evident in any of the other experiments. For divergence amplitude, the amplitude is lower than the consensus profile, but there is no oscillation in the lower layers of the atmosphere and the magnitude of the error is smaller, as it is for the FEM-A model. The FEM-B model profile is further from the consensus profile than the FEM-A model profile for temperature phase but it is still very close (Fig. 3.29). The profiles for divergence phase are identical for all four models (Fig. 3.28(bottom)).

2. Six-Layer Models

In the six-layer case the FDM-A, FDM-B, and FEM-A models all seem to converge to the same solution, but the FEM-B profile is off in the temperature amplitude and the divergence amplitude (Figs. 3.30 and 3.31) although the pattern is similar. The phase profiles for all four six-layer models are very close to the sixty-layer consensus. The FEM-A six-layer model profile for temperature amplitude is closer to the sixty-layer consensus than the FDM-A six-layer model and slightly better than the FDM-B six-layer model (Fig. 3.32). The temperature amplitude profile oscillation in the lowest layers of the FEM-B sixty-layer model is evident at $Z = 0.3$ in the six-layer model (Fig. 3.33). The reason for this oscillation is unclear, but it should have something to do with the basis functions near the boundaries.

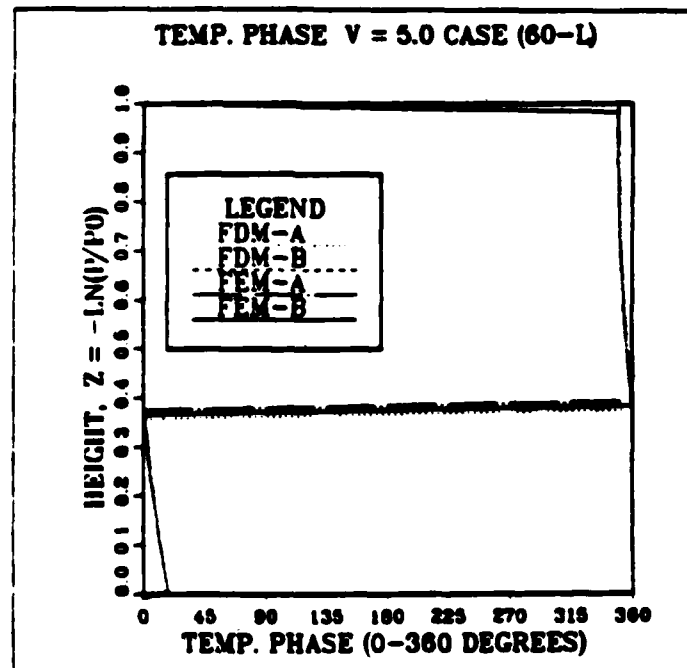
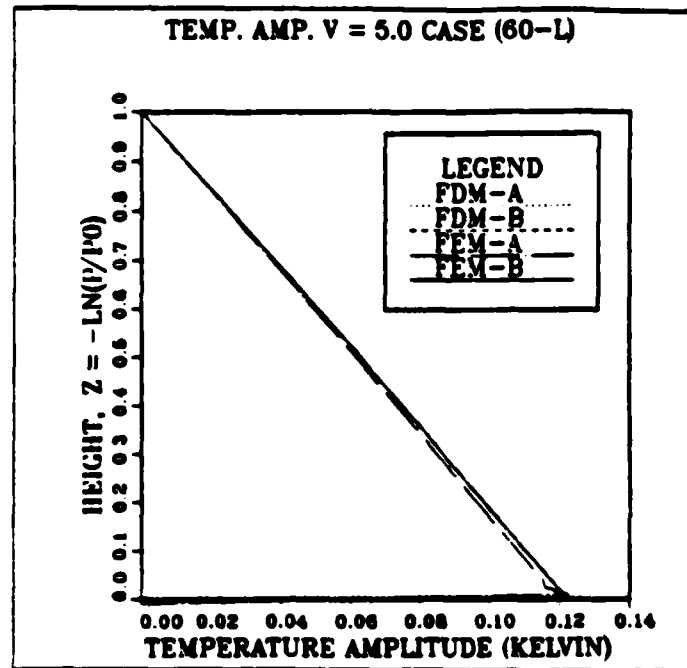


Fig. 3.1 Sixty-layer Rossby wave experiment at 96 hours. Temperature amplitude profiles (top) and temperature phase profiles (bottom) are compared.

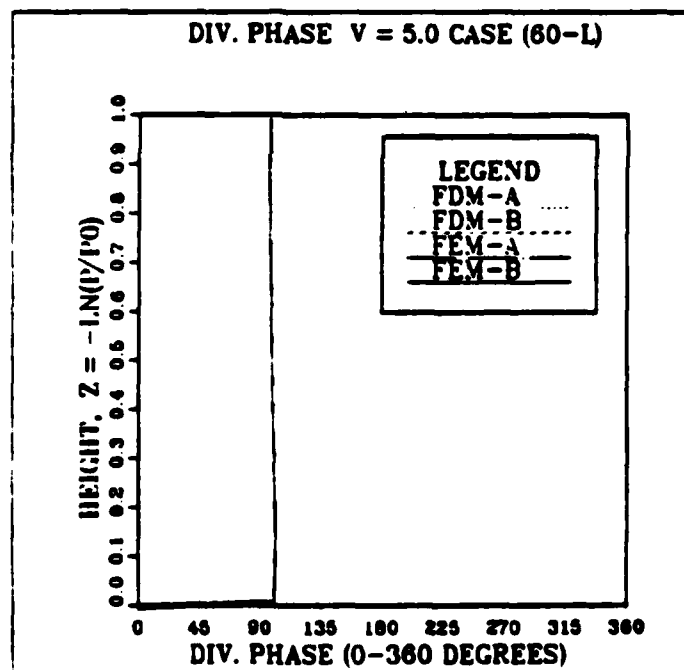
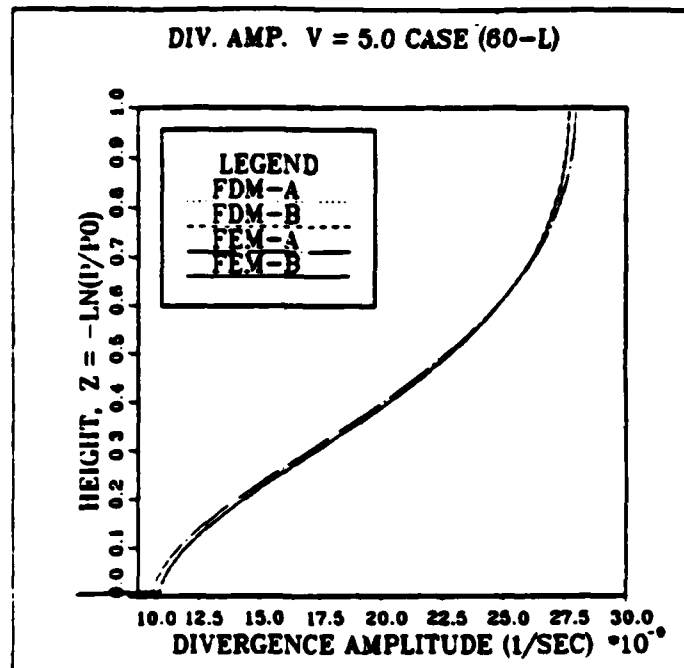


Fig. 3.2 Sixty-layer Rossby wave experiment at 96 hours. Divergence amplitude profiles (top) and divergence phase profiles (bottom) are compared.

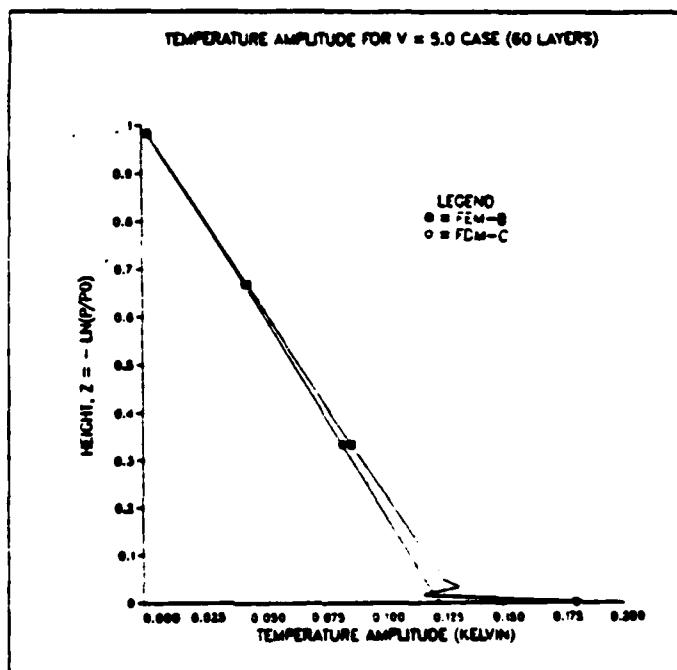
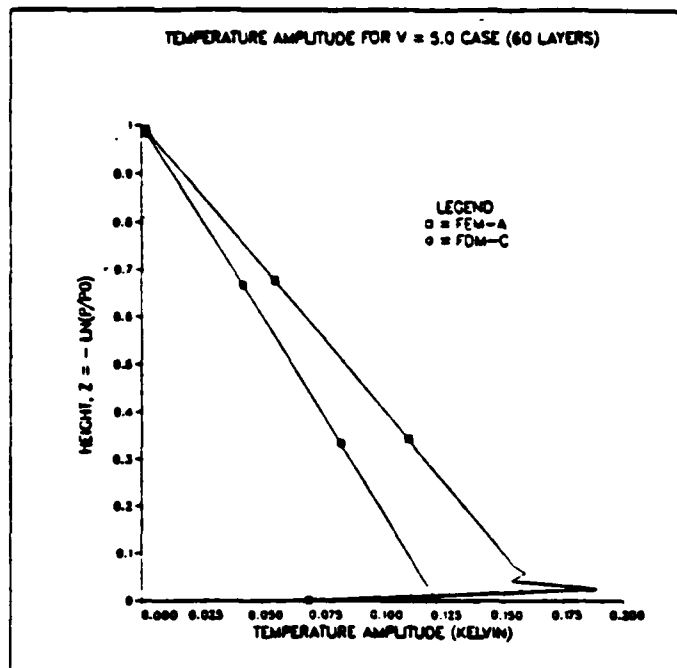


Fig. 3.3 Sixty-layer Rossby wave experiment at 96 hours from Jordan (1985). Temperature amplitude profiles are compared for models FEM-A (top) and FEM-B (bottom) and FDM-C, which represents the consensus profile.

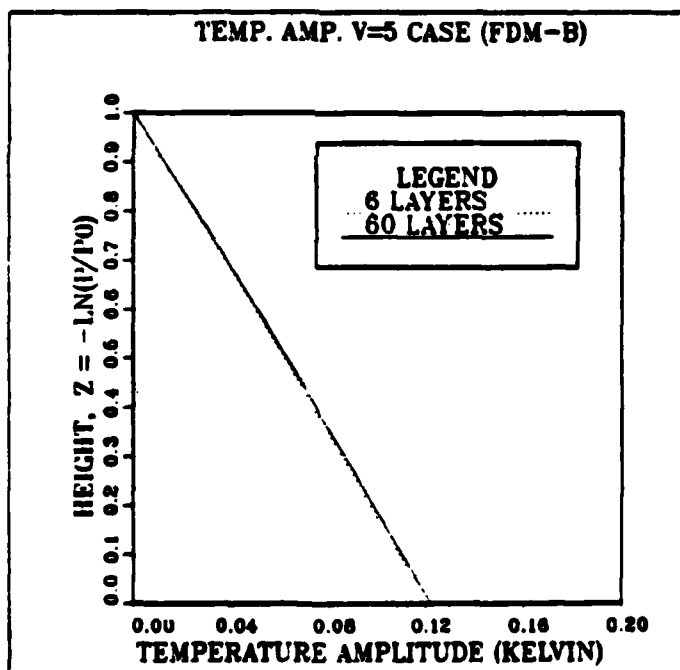
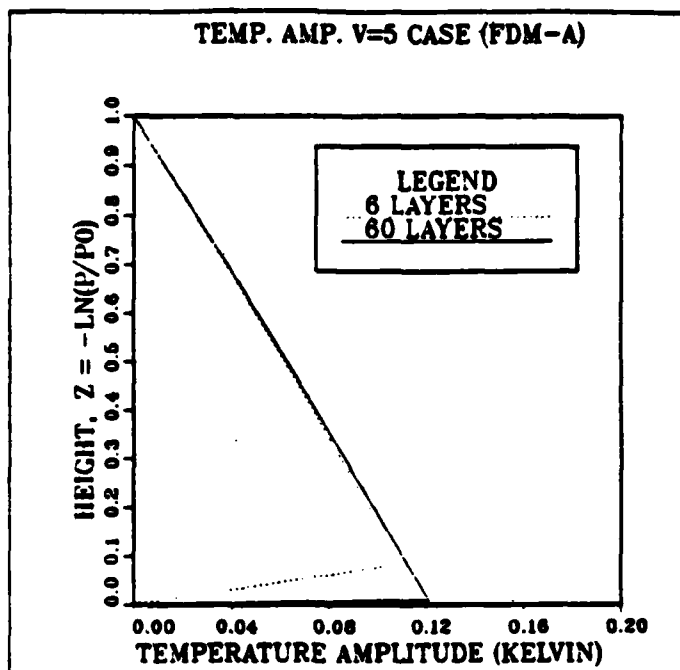


Fig. 3.4 Six-layer Rossby wave experiment at 96 hours. Temperature amplitude profiles are compared for the six-layer and sixty-layer FDM-A (top) and FDM-B (bottom) models.

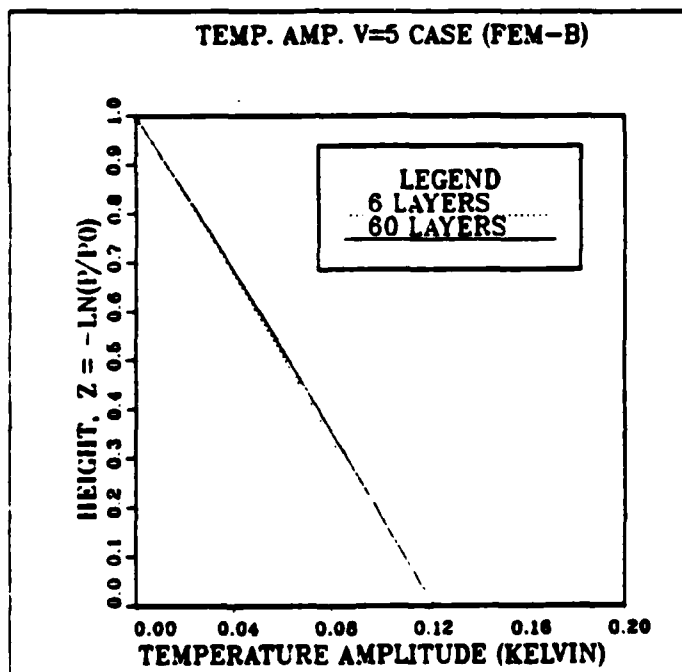
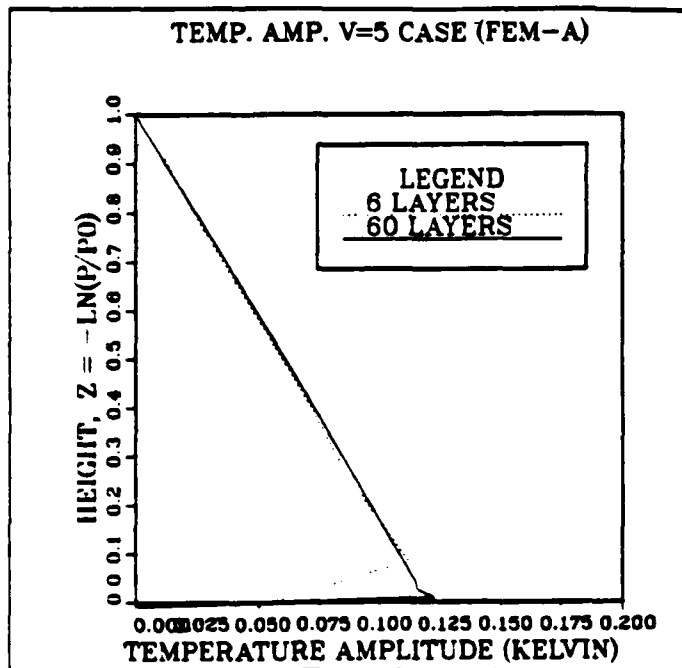


Fig. 3.5 Six-layer Rossby wave experiment at 96 hours. Temperature amplitude profiles are compared for the six-layer and sixty-layer FEM-A (top) and FEM-B (bottom) models.

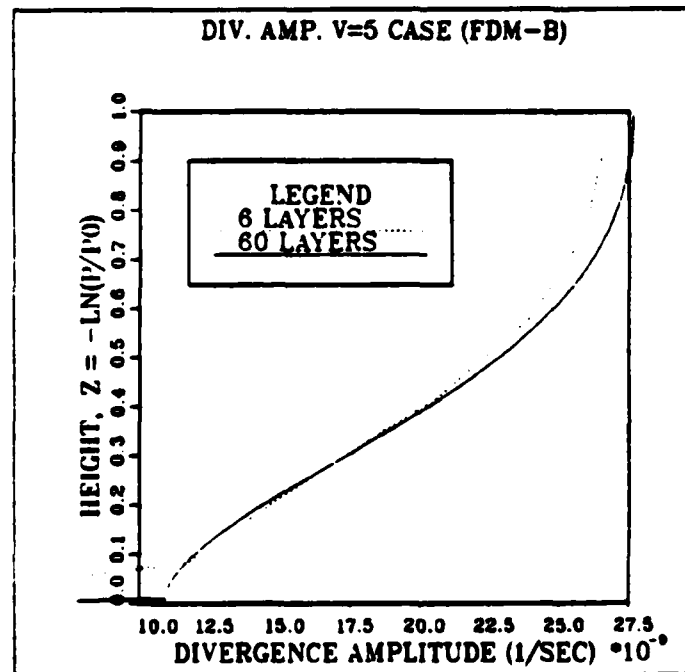
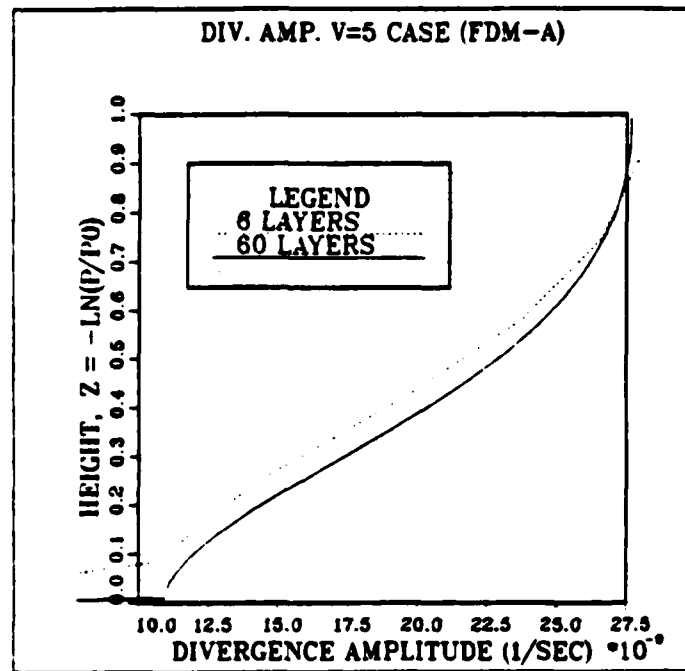


Fig. 3.6 Six-layer Rossby wave experiment at 96 hours. Divergence amplitude profiles are compared for the six-layer and sixty-layer FDM-A (top) and FDM-B (bottom) models.

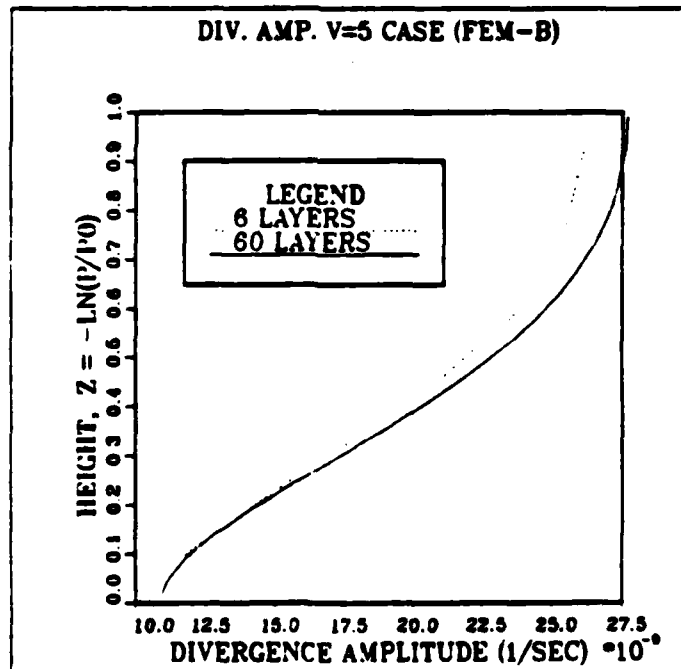
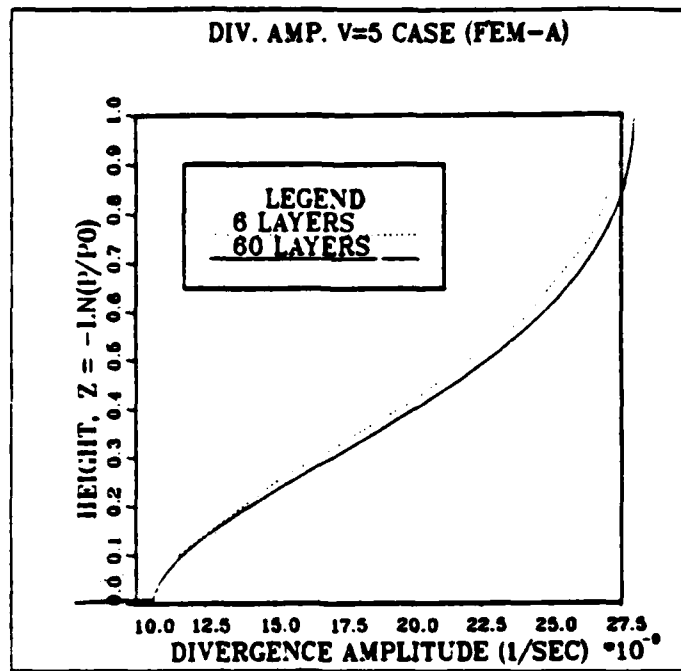


Fig. 3.7 Six-layer Rossby wave experiment at 96 hours. Divergence amplitude profiles are compared for the six-layer and sixty-layer FEM-A (top) and FEM-B (bottom) models.

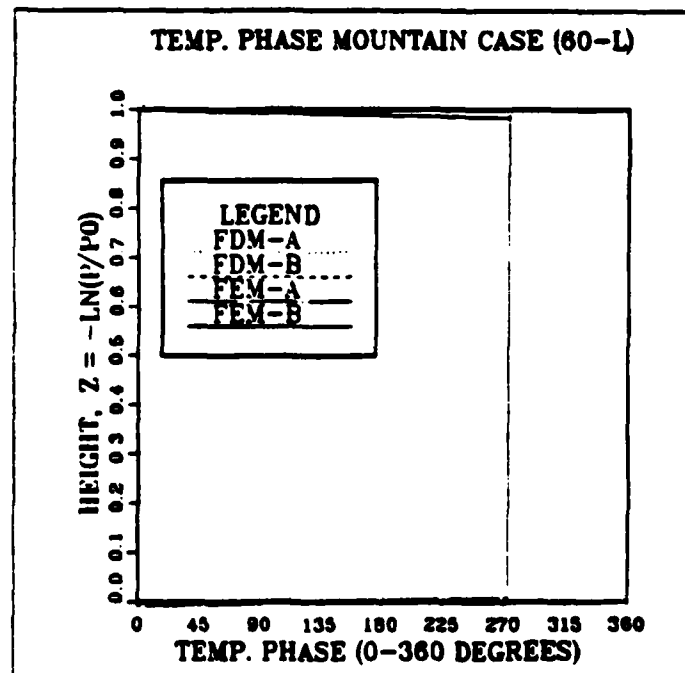
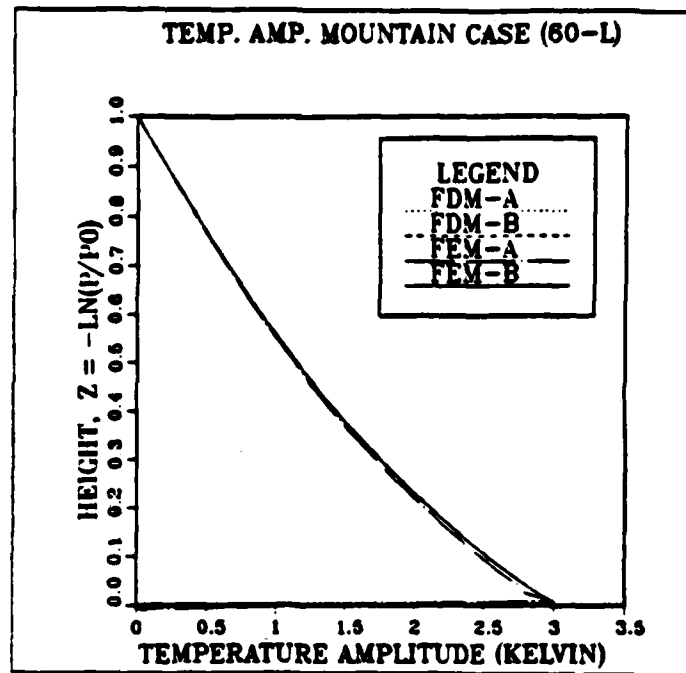


Fig. 3.8 Sixty-layer mountain topography experiment at 96 hours. Temperature amplitude profiles (top) and temperature phase profiles (bottom) are compared.

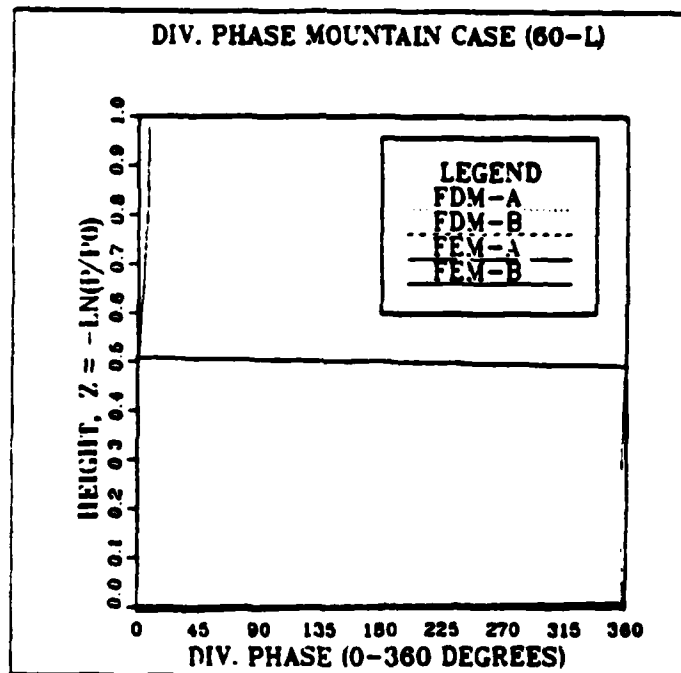
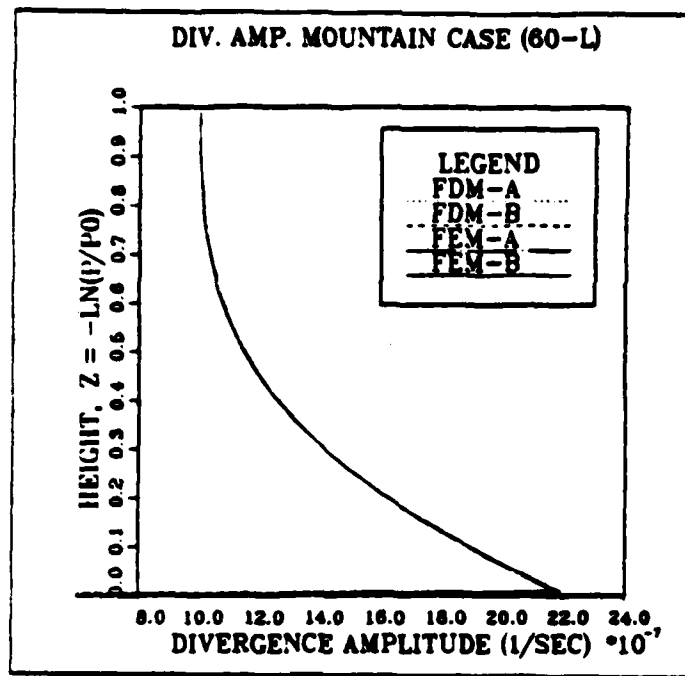


Fig. 3.9 Sixty-layer mountain topography experiment at 96 hours. Divergence amplitude profiles (top) and divergence phase profiles (bottom) are compared.

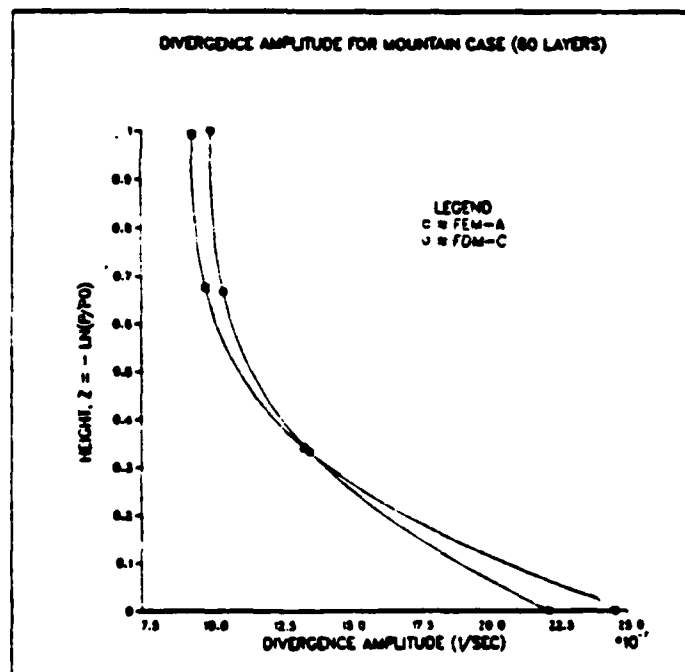
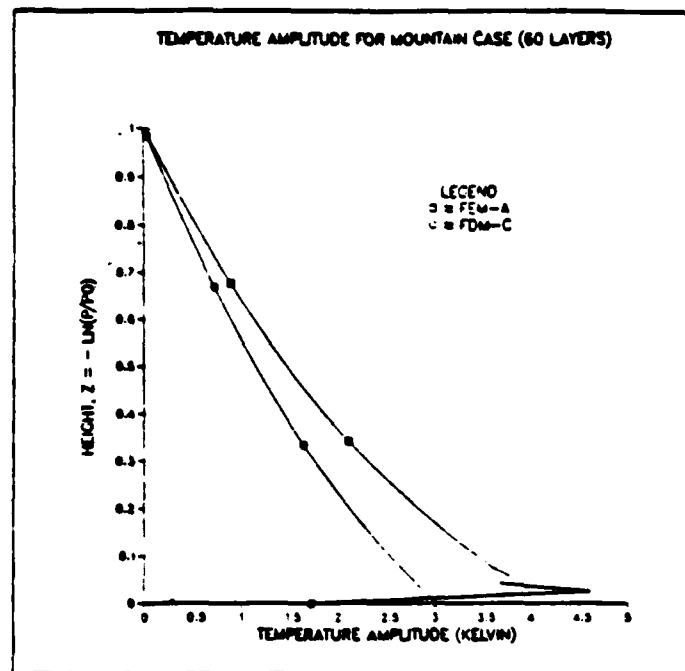


Fig. 3.10 Sixty-layer mountain topography experiment at 96 hours from Jordan (1985). Temp. (top) and divergence (bottom) amplitude profiles are compared for models FEM-A and FDM-C, which represents the consensus profile.

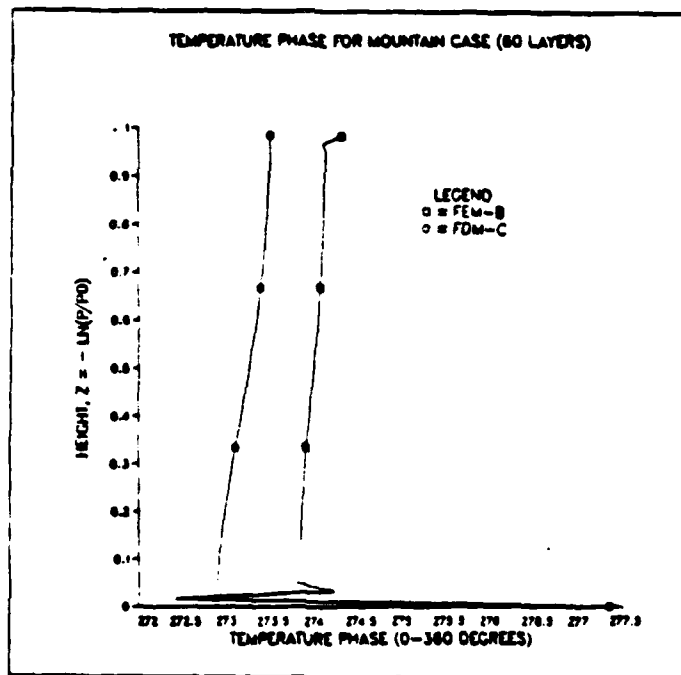
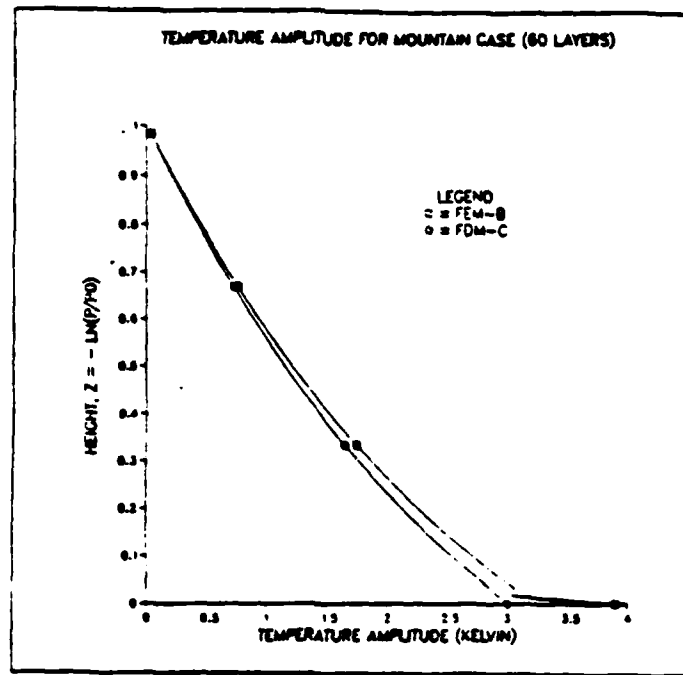


Fig. 3.11 Sixty-layer mountain topography experiment at 96 hours from Jordan (1985). Temperature amplitude (top) and phase (bottom) profiles are compared for models FEM-B and FDM-C, which represents the consensus profile.

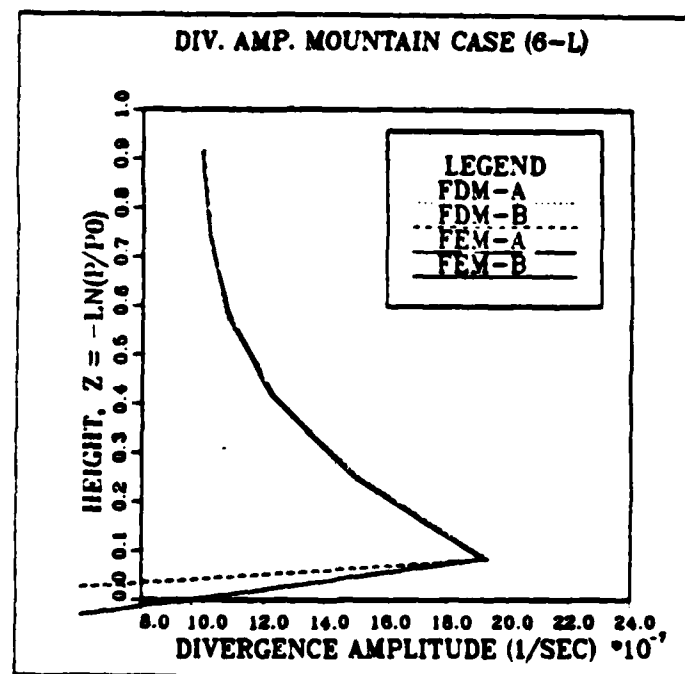
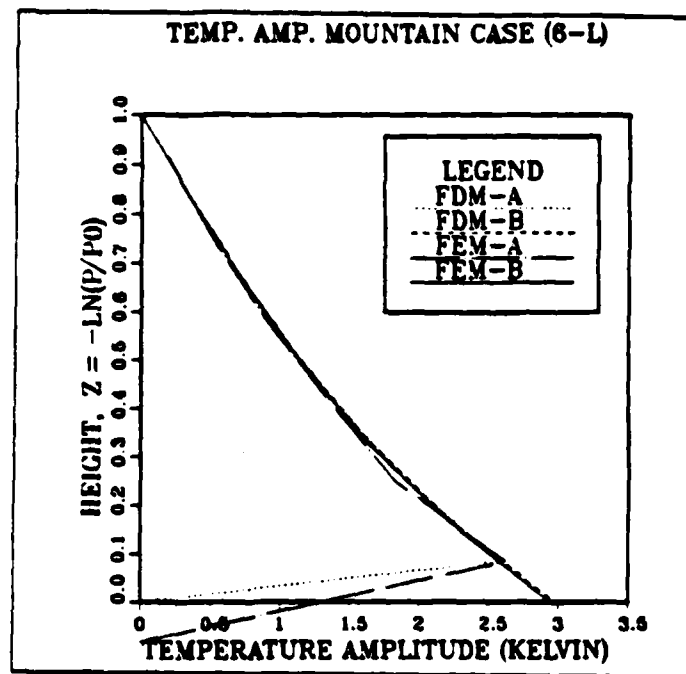


Fig. 3.12 Six-layer mountain topography experiment at 96 hours. Temperature amplitude profiles (top) and divergence amplitude profiles (bottom) are compared.

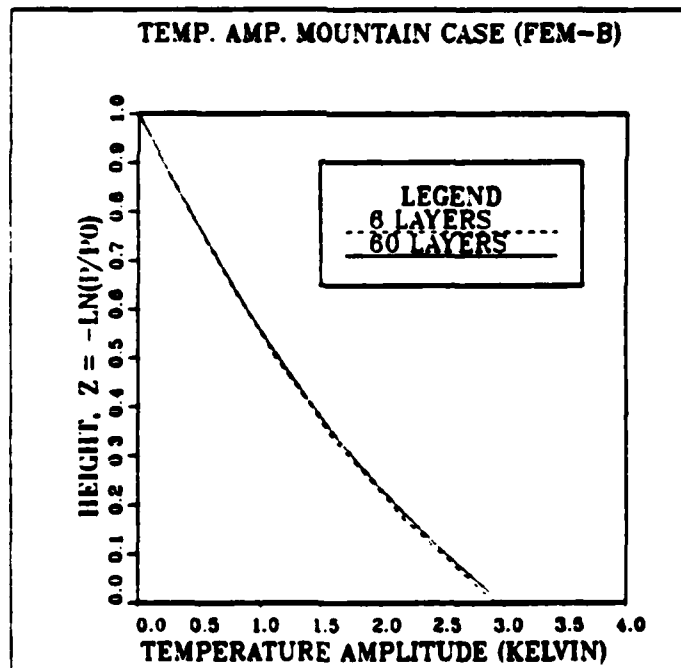
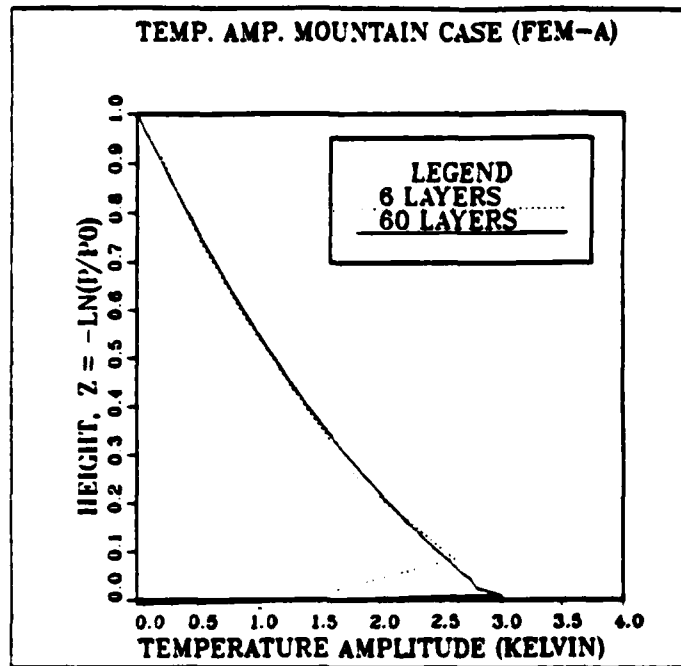


Fig. 3.13 Six-layer mountain topography experiment at 96 hours. Temperature amplitude profiles are compared for the six-layer and sixty-layer FEM-A (top) and FEM-B (bottom) models.

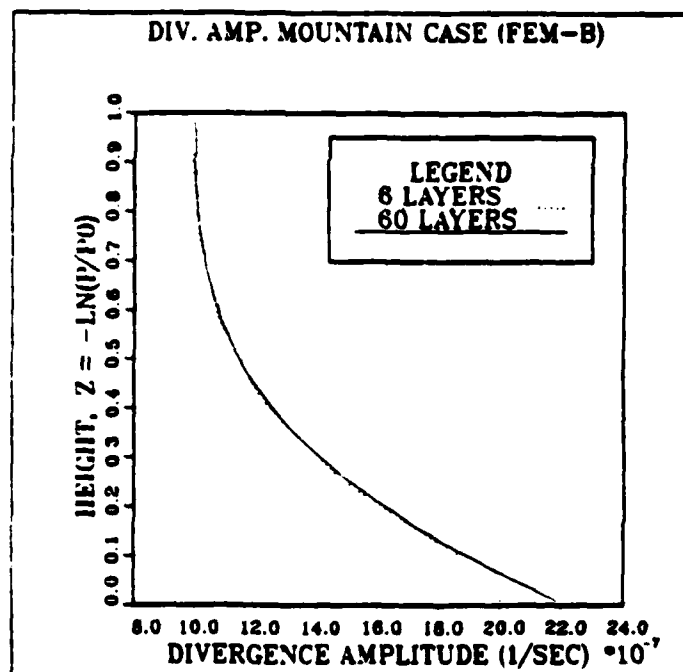
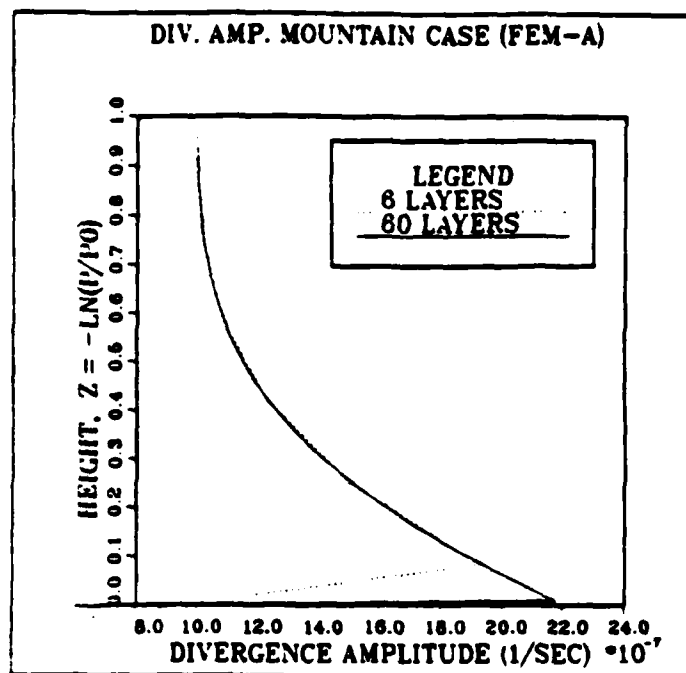


Fig. 3.14 Six-layer mountain topography experiment at 96 hours. Divergence amplitude profiles are compared for the six-layer and sixty-layer FEM-A (top) and FEM-B (bottom) models.

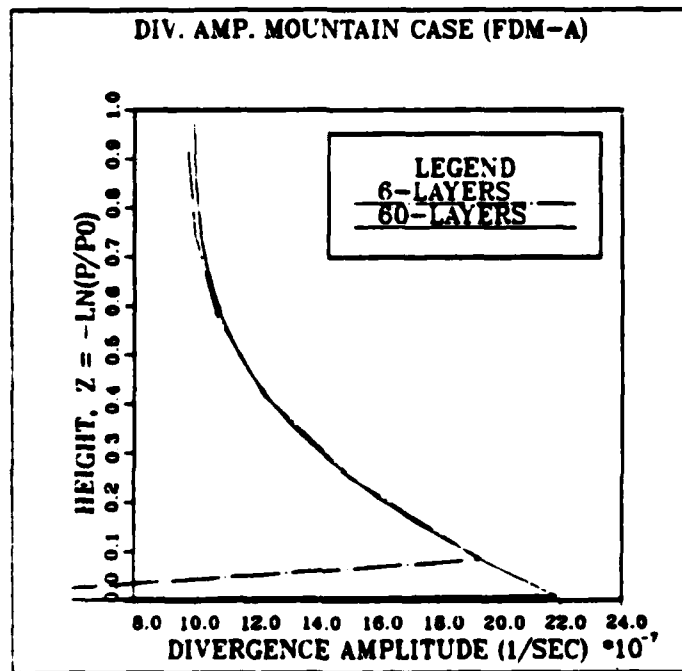


Fig. 3.15 Six-layer mountain topography experiment at 96 hours.
 Divergence amplitude profiles are compared for the six-layer
 and sixty-layer FDM-A model.

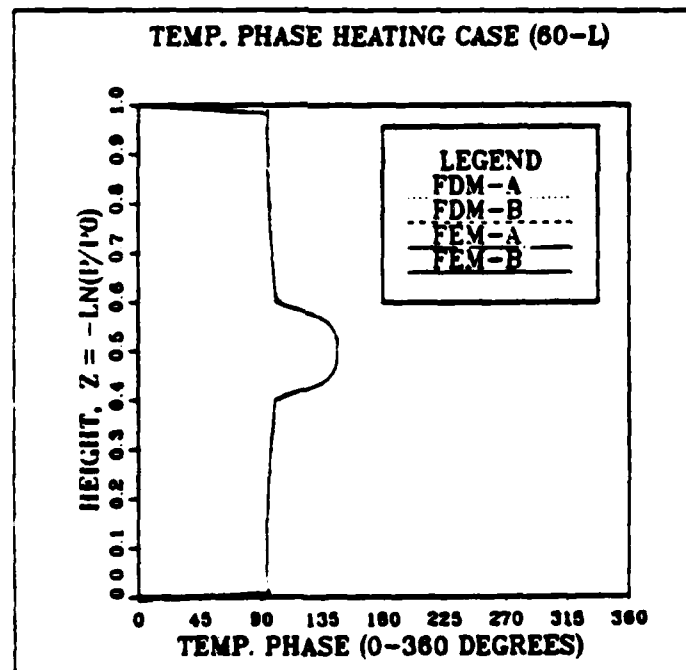
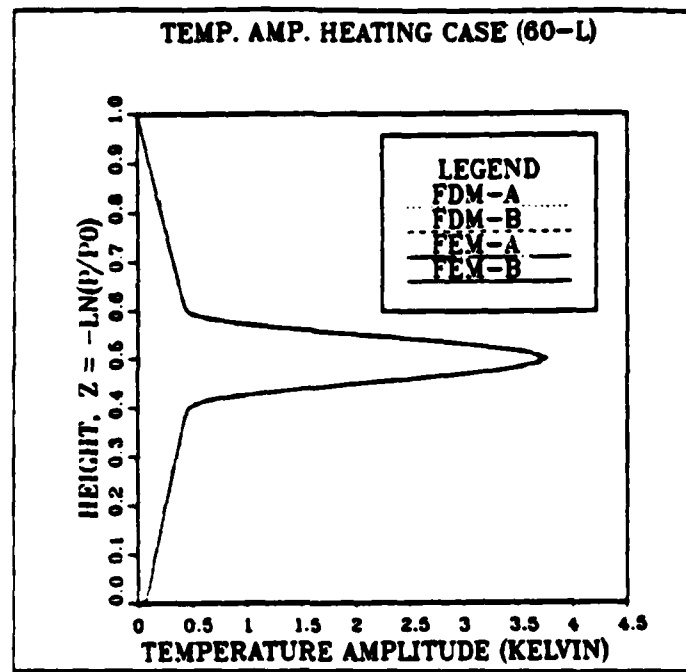


Fig. 3.16 Sixty-layer diabatic heating experiment at 96 hours. Temperature amplitude profiles (top) and temperature phase profiles (bottom) are compared.

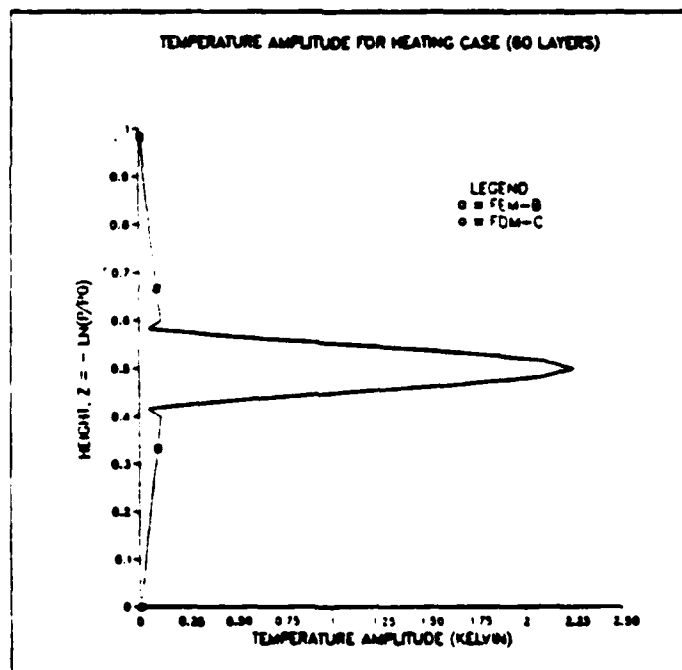
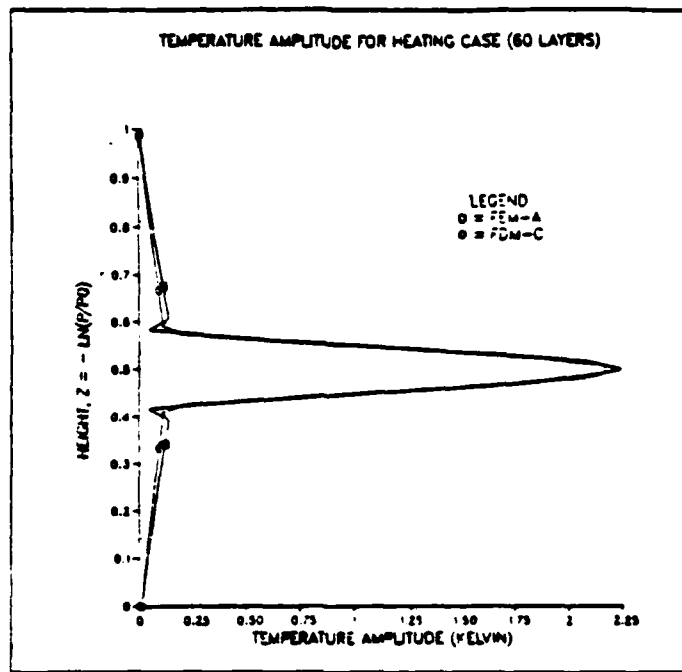


Fig. 3.17 Sixty-layer diabatic heating experiment at 12 hours from Jordan (1985). Temperature amplitude profiles are compared for models FEM-A (top) and FEM-B (bottom) and FDM-C, which represents the consensus profile.

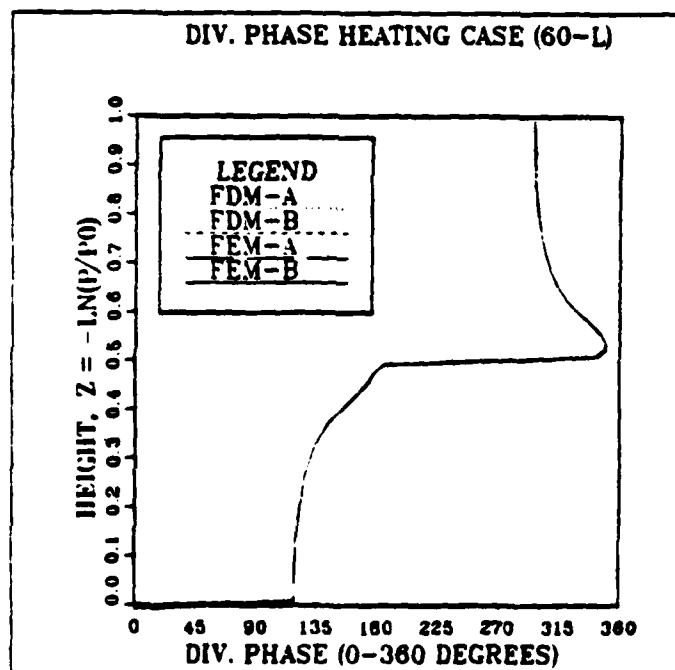
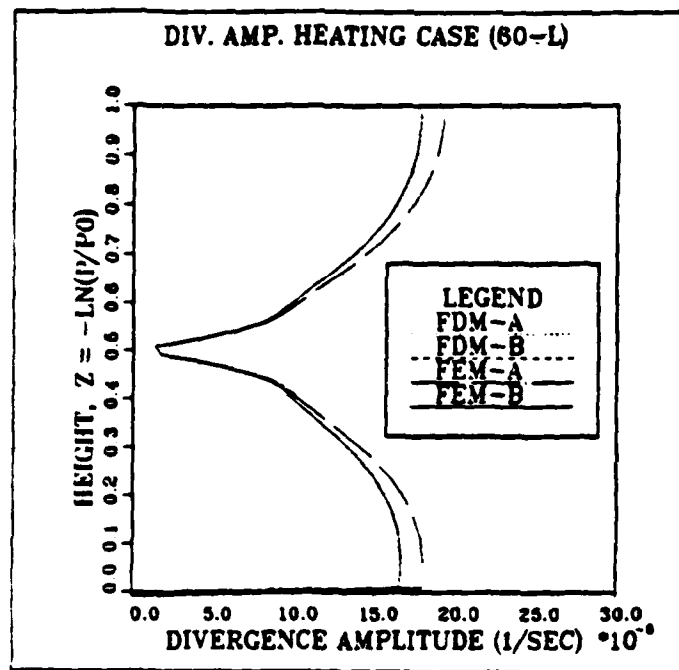


Fig. 3.18 Sixty-layer diabatic heating experiment at 96 hours.
 Divergence amplitude profiles (top) and divergence phase
 profiles (bottom) are compared.

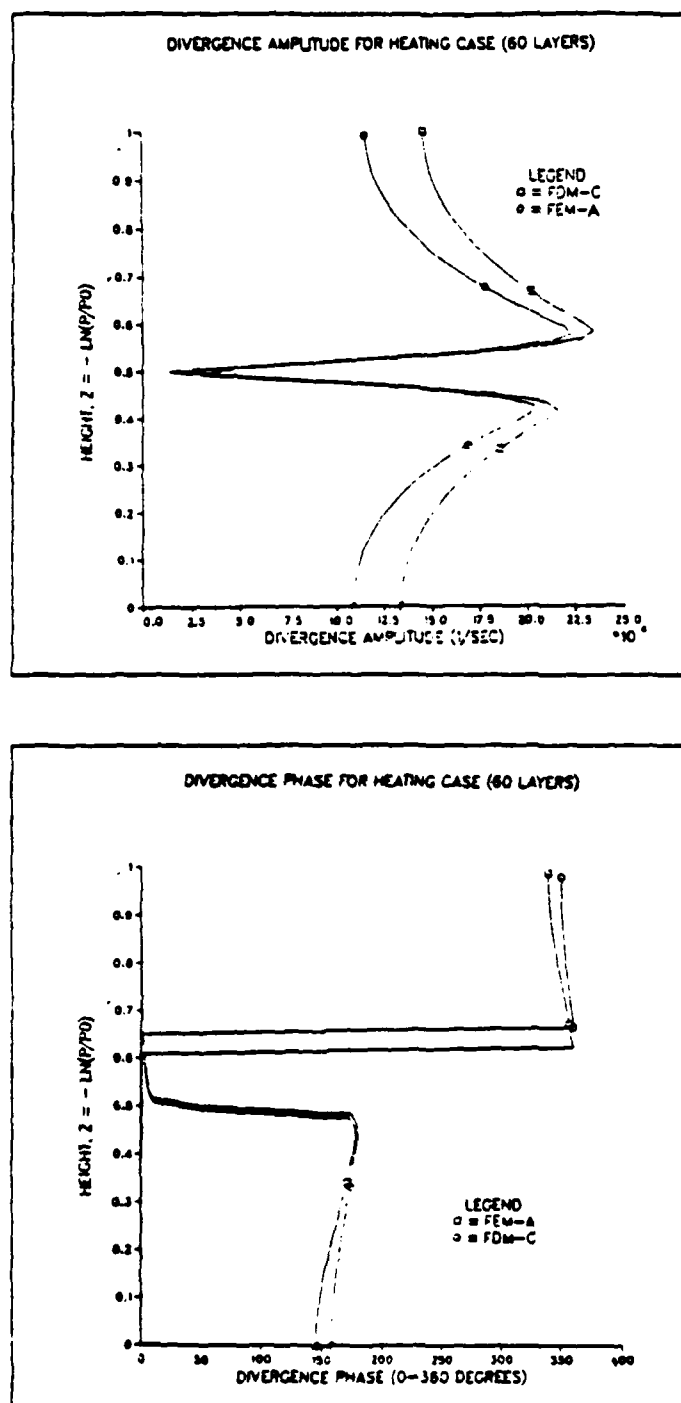


Fig. 3.19 Sixty-layer diabatic heating experiment at 12 hours from Jordan (1985). Divergence amplitude (top) and phase (bottom) profiles are compared for models FEM-A and FDM-C, which represents the consensus profile.

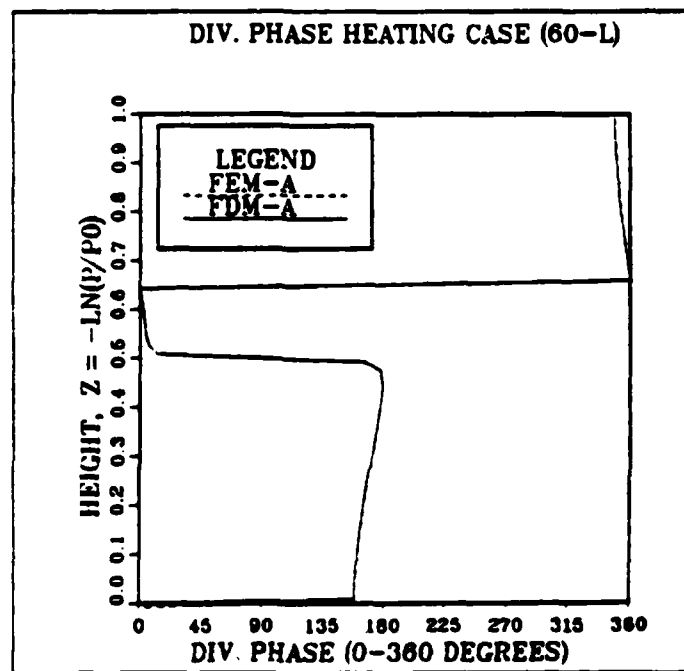


Fig. 3.20 Sixty-layer diabatic heating experiment at 12 hours. divergence phase profiles are compared for models FEM-A and FDM-A, which represents the consensus profile.

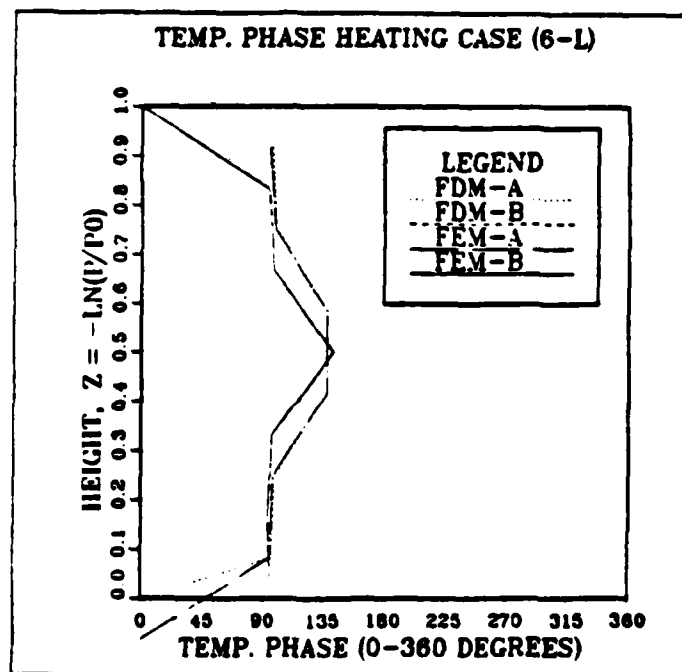
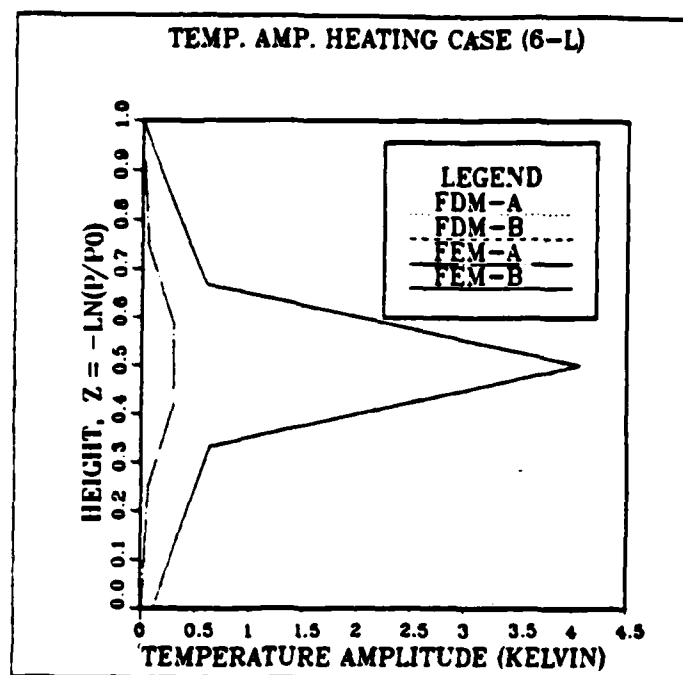


Fig. 3.21 Six-layer diabatic heating experiment at 96 hours. Temperature amplitude profiles (top) and temperature phase profiles (bottom) are compared.

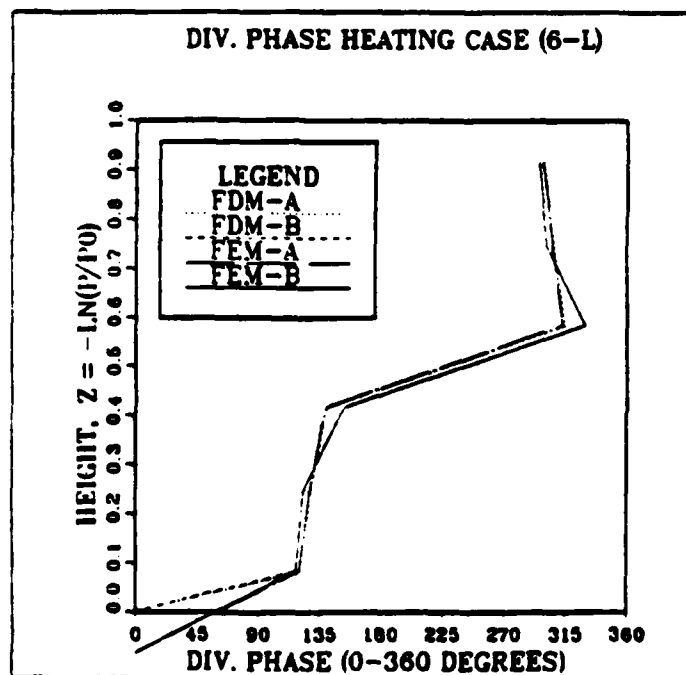
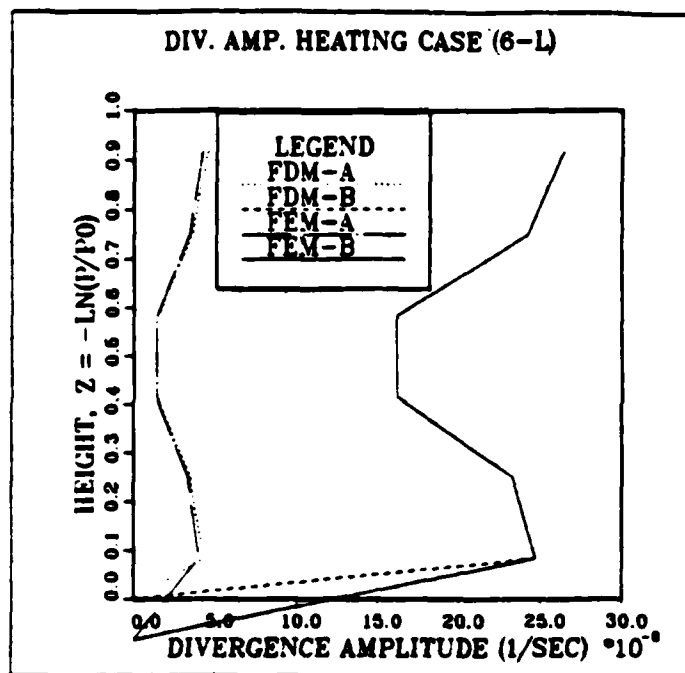


Fig. 3.22 Six-layer diabatic heating experiment at 96 hours. Divergence amplitude profiles (top) and divergence phase profiles (bottom) are compared.

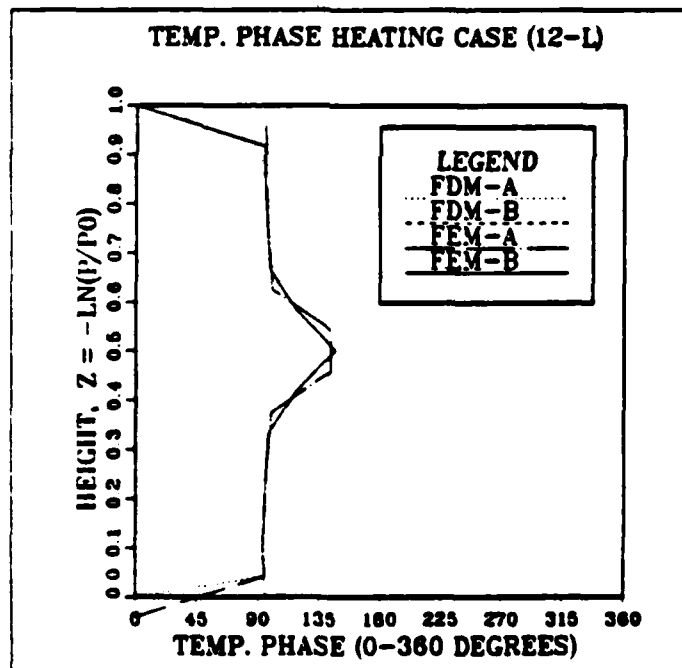
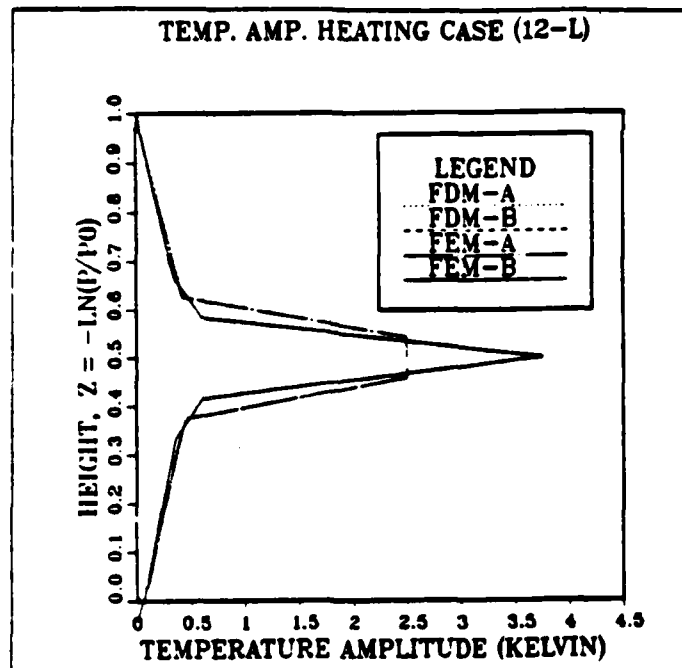


Fig. 3.23 Twelve-layer diabatic heating experiment at 96 hours. Temperature amplitude profiles (top) and temperature phase profiles (bottom) are compared.

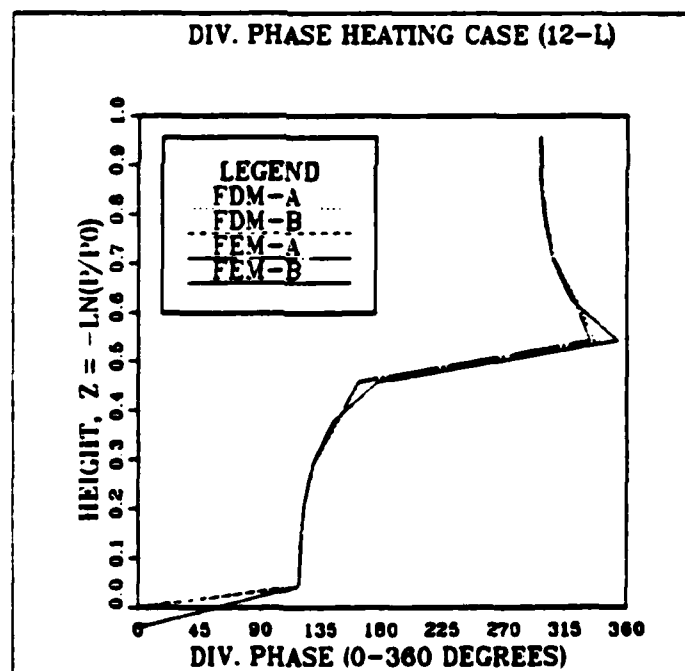
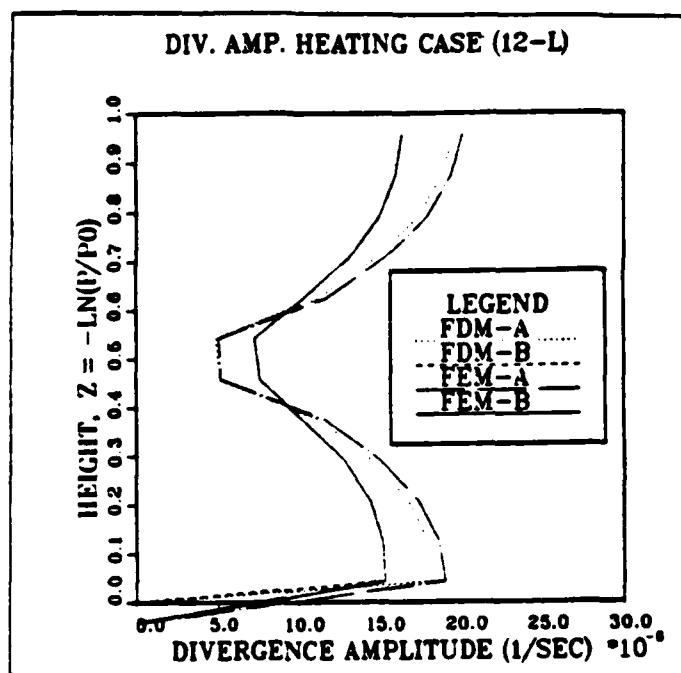


Fig. 3.24 Twelve-layer diabatic heating experiment at 96 hours. Divergence amplitude profiles (top) and divergence phase profiles (bottom) are compared.

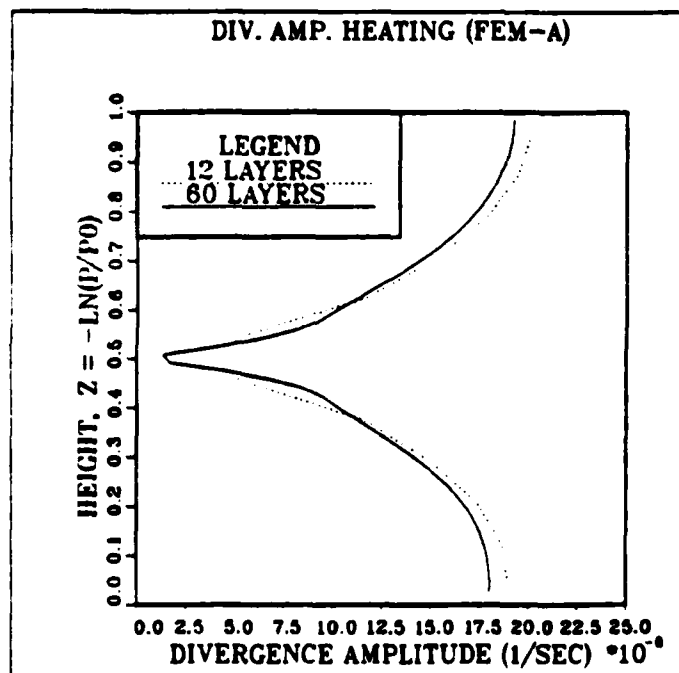
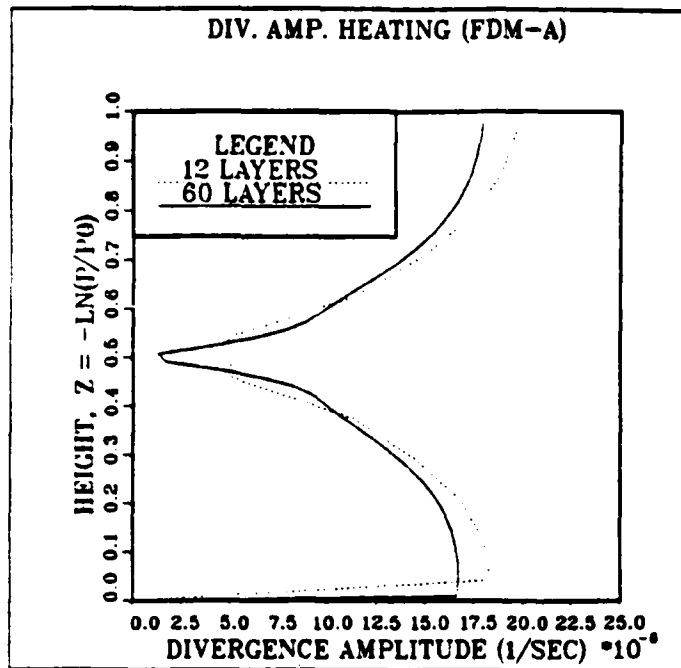


Fig. 3.25 Twelve-layer diabatic heating experiment at 96 hours. Divergence amplitude profiles are compared for the twelve-layer and sixty-layer FDM-A (top) and FEM-A (bottom) models.

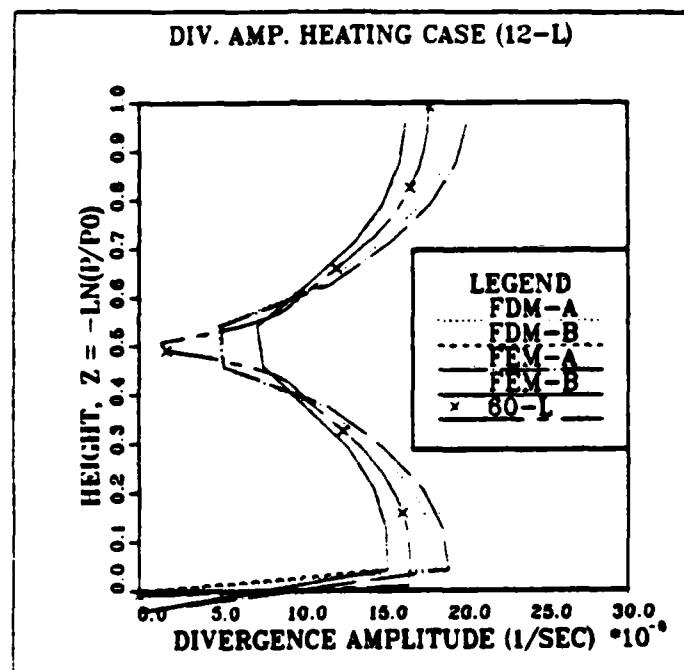


Fig. 3.26 Twelve-layer diabatic heating experiment at 96 hours. Divergence amplitude profiles are compared for models FDM-A, FDM-B, FEM-A, FEM-B and sixty-layer FEM-B, which represents the consensus profile.

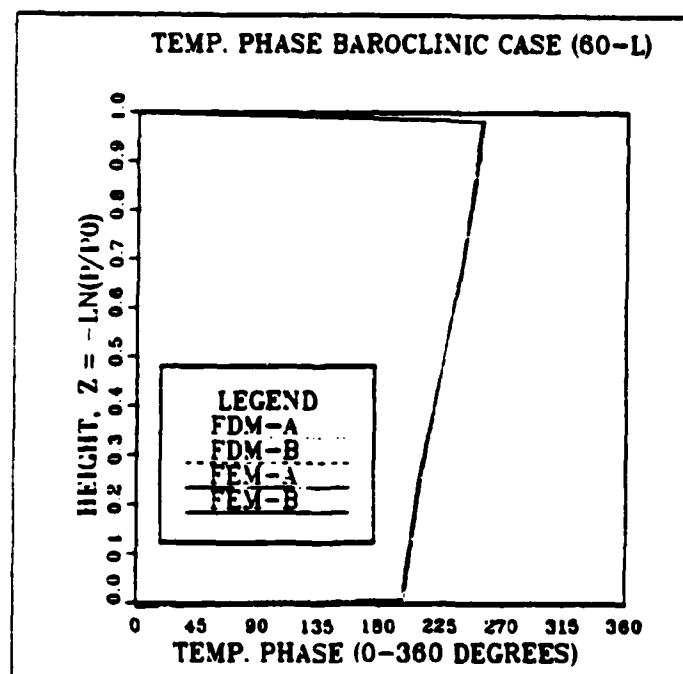
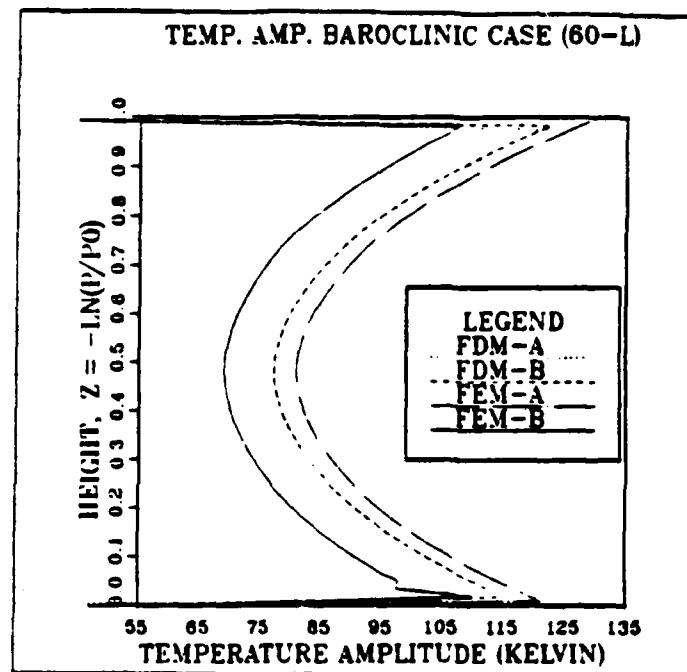


Fig. 3.27 Sixty-layer baroclinic instability experiment at 96 hours. Temperature amplitude profiles (top) and temperature phase profiles (bottom) are compared.

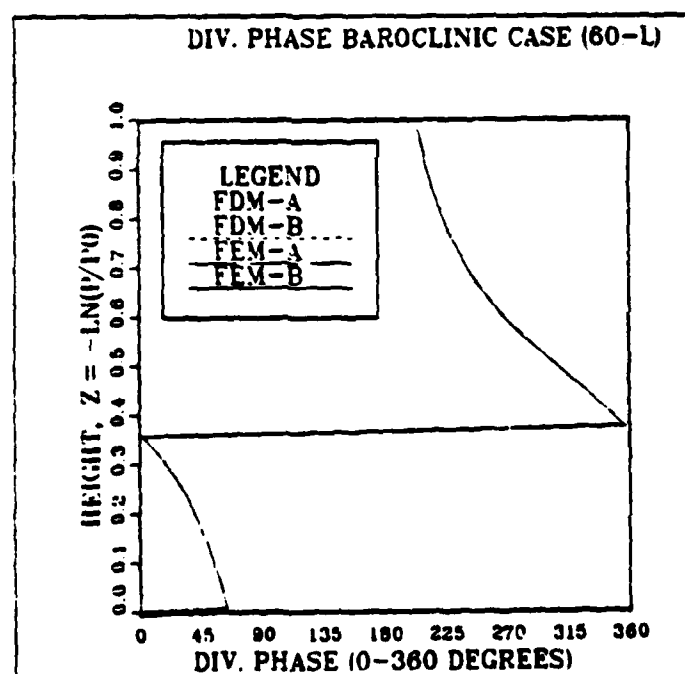
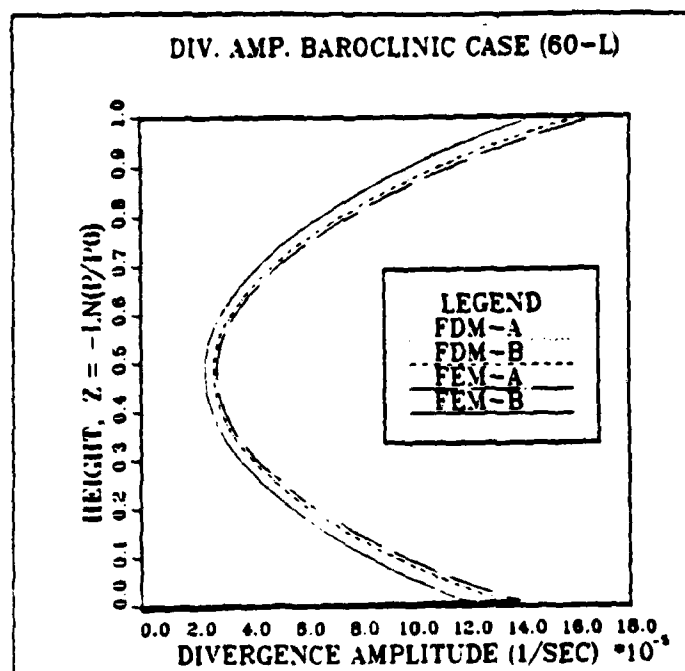


Fig. 3.28 Sixty-layer baroclinic instability experiment at 96 hours. Divergence amplitude profiles (top) and divergence phase profiles (bottom) are compared.

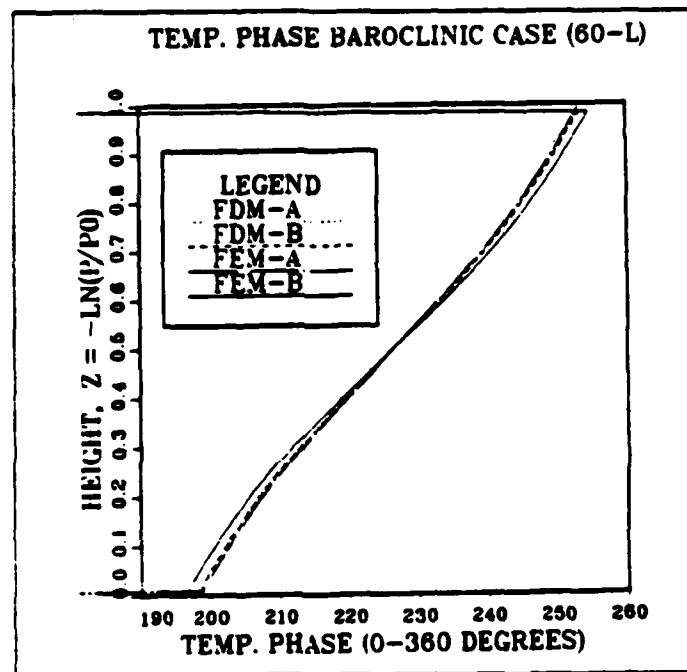


Fig. 3.29 Sixty-layer baroclinic instability experiment at 96 hours.
 Temperature phase profiles are compared on a closer scale.
 Compare Fig. 3.27(bottom).

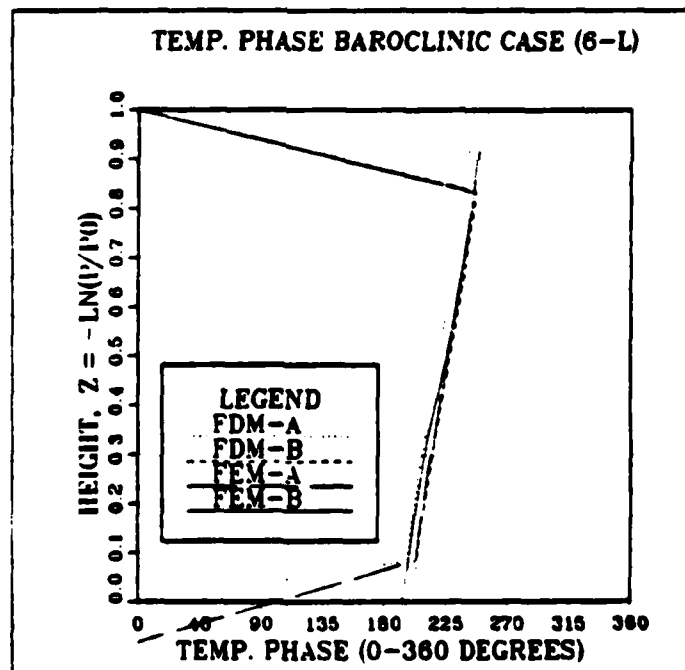
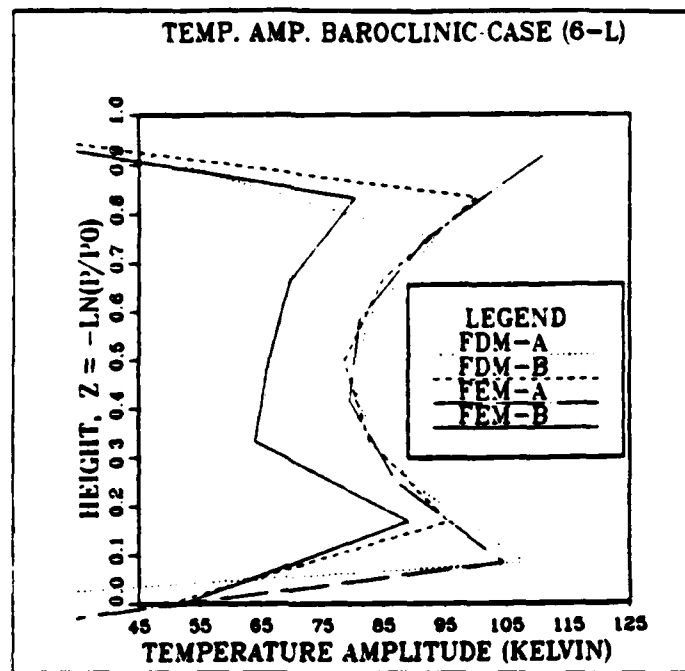


Fig. 3.30 Six-layer baroclinic instability experiment at 96 hours. Temperature amplitude profiles (top) and temperature phase profiles (bottom) are compared.

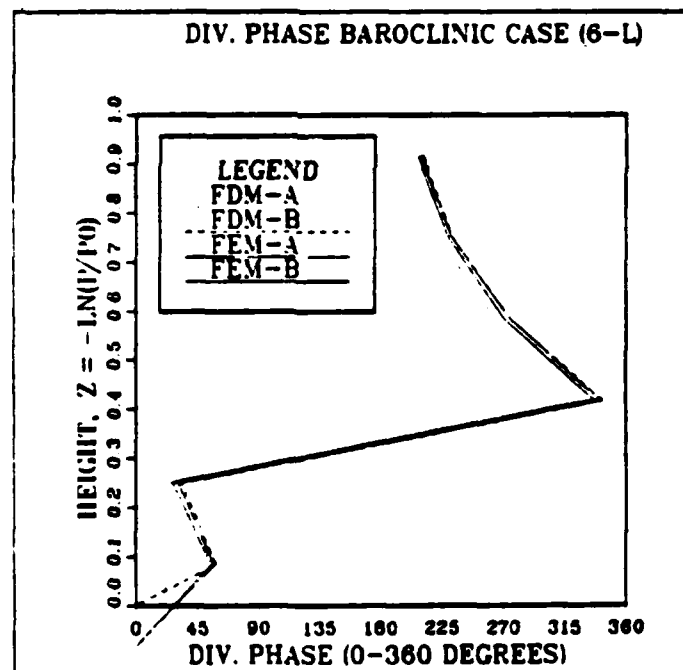
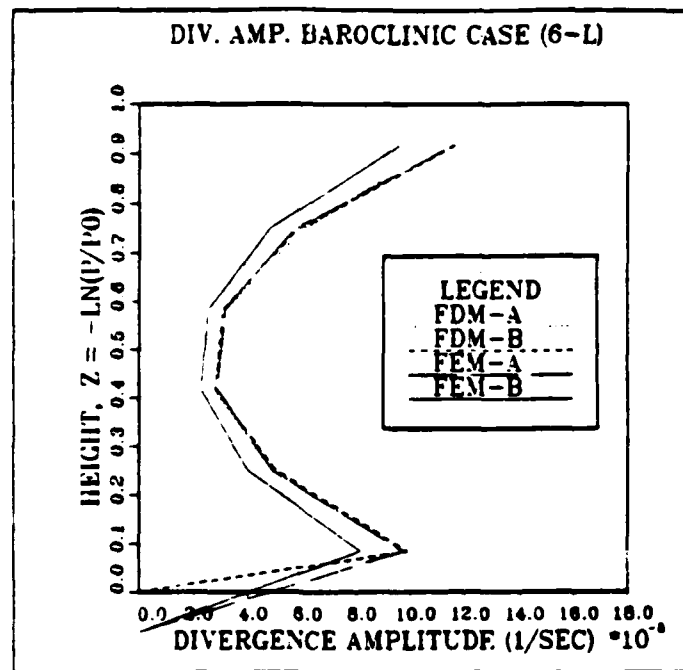


Fig. 3.31 Six-layer baroclinic instability experiment at 96 hours. Divergence amplitude profiles (top) and divergence phase profiles (bottom) are compared.

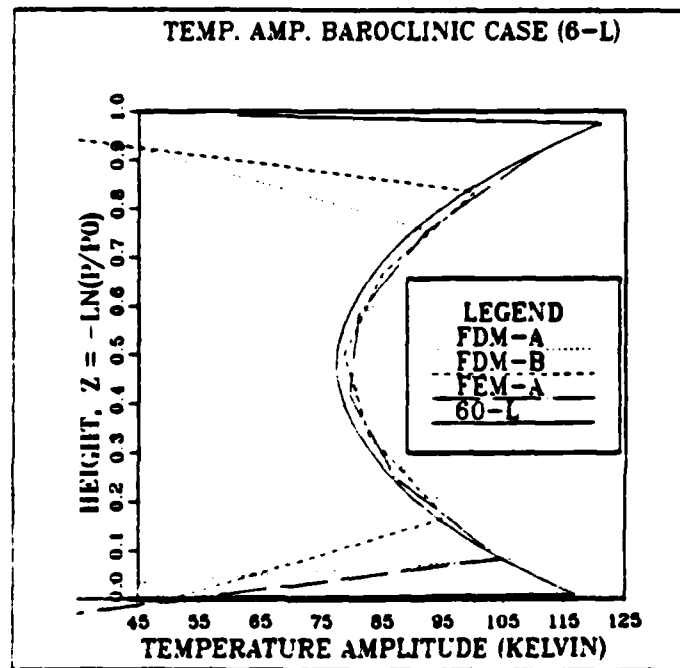


Fig. 3.32 Six-layer baroclinic instability experiment at 96 hours. Temperature amplitude profiles are compared for models FDM-A, FDM-B, FEM-A, and sixty-layer FDM-A, which represents the consensus profile.

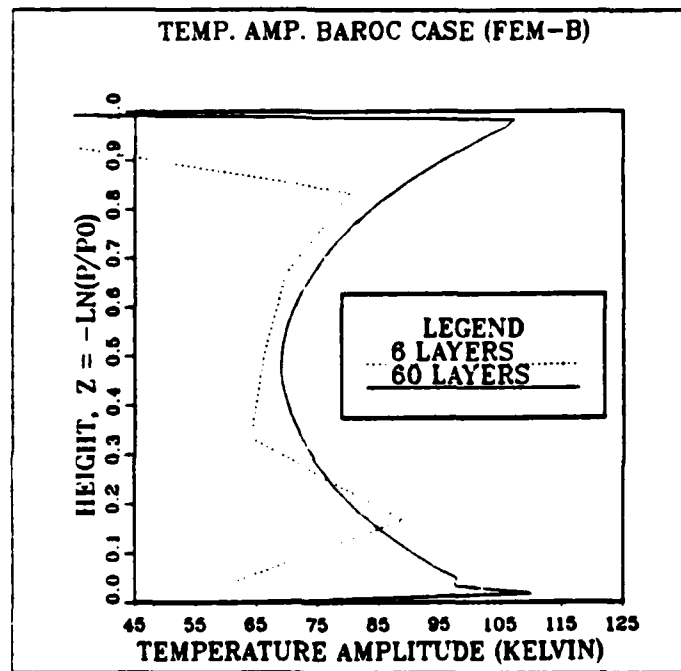


Fig. 3.33 Six-layer baroclinic instability experiment at 96 hours. Temperature amplitude profiles are compared for the six-layer and sixty-layer FEM-B model.

IV. CONCLUSIONS

The modification of the finite element models with the inclusion of the basis functions near the boundaries ($\phi_1(Z)$ and $\phi_{n+2}(Z)$) completely fixed the FEM-B model in the experiments that can be compared with the results of Jordan (1985). The modified FEM-A model is much better when compared with the results of the unmodified model, however the unusual temperature amplitude behavior in the lowest layers of the model are not totally gone after the modifications. The theory of Jordan (1985) that the oscillation in the temperature profiles of both unmodified models is generated by matrix elements which represent the contributions from the basis functions near the surface, is well supported by the results of the modified models. There is still some question as to how to define terms at or below the bottom of the atmosphere and a change in the definition of those terms may fix the small oscillations that are evident in the FEM-A model in the Rossby wave and mountain topography experiment.

The finite element models display a better convergence to the sixty-layer consensus than the finite difference models in many of the cases and in the other cases they are the same.

Jagged temperature profiles are not observed in the diabatic heating experiment in either the modified or the unmodified (Jordan, 1985) models. This may be because the heating is defined far enough away from the boundaries that the previous problems associated with the boundary terms are not significant. The FEM-A model has a slightly different sixty-layer divergence amplitude response outside the heated layer than the other models. The differences between grids is most apparent in this experiment. The differences may be caused by the difference in the maximum amplitude of the heating defined for the different grids. The results may be much closer if the maximum heating were to be set equal for both grids. This is supported by the fact that the sixty-layer profiles of all four models represent the same physical solution.

Both of the finite element model results differ from the consensus results for the baroclinic instability experiment for temperature and divergence amplitudes. The FEM-A model difference is probably a manifestation of the problems observed in the Rossby wave experiment and the mountain topography experiment. There is an oscillation and

a difference from the consensus in the baroclinic instability experiment for the FEM-B model which may also be caused by the definition of terms at or below the bottom of the atmosphere. In future studies the temperature on the boundary in the FEM-B model should be included in the forecast field. This may improve the behavior for the baroclinic experiments, where the surface temperature is very important.

APPENDIX A

FINITE DIFFERENCE APPROXIMATIONS

1. For terms of the form $\frac{d\bar{u}}{dZ} W$:

a. FDM-A and FDM-B, at level $Z = Z_i$:

$$\frac{d\bar{u}}{dZ} W = \frac{1}{2} \left\{ W_i \left(\frac{\bar{u}_{i+1} - \bar{u}_i}{Z_{i+1} - Z_i} \right) + W_{i-1} \left(\frac{\bar{u}_i - \bar{u}_{i-1}}{Z_i - Z_{i-1}} \right) \right\}$$

2. For terms of the form $\frac{\partial \bar{T}}{\partial Z} W$:

a. FDM-A at level $Z = Z_i$:

$$\frac{d\bar{T}}{dZ} W = \frac{1}{2} \left\{ W_i \left(\frac{\bar{T}_{i+1} - \bar{T}_i}{Z_{i+1} - Z_i} \right) + W_{i-1} \left(\frac{\bar{T}_i - \bar{T}_{i-1}}{Z_i - Z_{i-1}} \right) \right\}$$

b. FDM-B at level $Z = Z_i$:

$$\frac{d\bar{T}}{dZ} W = \frac{1}{2} W_i \left\{ \left(\frac{\bar{T}_{i+1} - \bar{T}_i}{Z'_{i+1} - Z'_i} \right) + \left(\frac{\bar{T}_i - \bar{T}_{i-1}}{Z'_i - Z'_{i-1}} \right) \right\}$$

3. For terms of the form $\frac{d\bar{u}}{dZ} V$:

a. FDM-A, at level $Z = Z_i$:

$$\frac{d\bar{u}}{dZ} V = \frac{1}{2} V_i \left\{ \left(\frac{\bar{u}_{i+1} - \bar{u}_i}{Z_{i+1} - Z_i} \right) + \left(\frac{\bar{u}_i - \bar{u}_{i-1}}{Z_i - Z_{i-1}} \right) \right\}$$

b. FDM-B, at level $Z = Z'_i$:

$$\frac{d\bar{u}}{dZ} V = \frac{1}{2} (V_{i+1} + V_i) \left(\frac{\bar{u}_{i+1} - \bar{u}_i}{Z_{i+1} - Z_i} \right)$$

APPENDIX B

GALERKIN FORM OF FEM-A PROGNOSTIC EQUATIONS

1. Vorticity Equations (2.25) and (2.26) :

$$\begin{aligned}
 \sum_{j=i-1}^{i+1} \frac{dA_1^j}{dt} \int_{Z_0}^{Z_T} \phi_j \phi_i dZ &= -f \sum_{j=i-1}^{i+1} D_1^j \int_{Z_0}^{Z_T} \phi_j \phi_i dZ \\
 - \mu \sum_{k=i-1}^{i+1} \bar{u}^k \sum_{j=i-1}^{i+1} A_2^j \int_{Z_0}^{Z_T} \phi_j \phi_k \phi_i dZ \\
 - \beta \sum_{j=i-1}^{i+1} v_1^j \int_{Z_0}^{Z_T} \phi_j \phi_i dZ .
 \end{aligned} \tag{B.1}$$

$$\begin{aligned}
 \sum_{j=i-1}^{i+1} \frac{dA_2^j}{dt} \int_{Z_0}^{Z_T} \phi_j \phi_i dZ &= -f \sum_{j=i-1}^{i+1} D_2^j \int_{Z_0}^{Z_T} \phi_j \phi_i dZ \\
 + \mu \sum_{k=i-1}^{i+1} \bar{u}^k \sum_{j=i-1}^{i+1} A_1^j \int_{Z_0}^{Z_T} \phi_j \phi_k \phi_i dZ \\
 - \beta \sum_{j=i-1}^{i+1} v_2^j \int_{Z_0}^{Z_T} \phi_j \phi_i dZ .
 \end{aligned} \tag{B.2}$$

Note that in these equations, and the equations that follow, the basis functions are functions of Z ($\phi_i = \phi_i(Z)$ and $\psi_i = \psi_i(Z)$). All of the other variables, A , D , H , Q , T , u , U , V , and W , are functions of time ($A_i = A_i(t)$, $D_i = D_i(t)$, $H_i = H_i(t)$, $Q_i = Q_i(t)$, $T_i = T_i(t)$, $u = u(t)$, $U_i = U_i(t)$, $V_i = V_i(t)$, $W_i = W_i(t)$).

2. Divergence Equations (2.27) and (2.28) :

$$\begin{aligned}
 \sum_{j=i-1}^{i+1} \frac{dD_j^1}{dt} \int_{Z_0}^{Z_T} \varphi_j \varphi_i dZ &= \int \sum_{j=i-1}^{i+1} A_j^1 \int_{Z_0}^{Z_T} \varphi_j \varphi_i dZ \\
 - \mu \sum_{k=i-1}^{i+1} \bar{u}^k \sum_{j=i-1}^{i+1} D_j^2 \int_{Z_0}^{Z_T} \varphi_j \varphi_k \varphi_i dZ \\
 - \beta \sum_{j=i-1}^{i+1} U_j^1 \int_{Z_0}^{Z_T} \varphi_j \varphi_i dZ . \\
 - \mu \sum_{k=i-1}^{i+1} \bar{u}^k \sum_{j=i-1}^{i+1} W_j^2 \int_{Z_0}^{Z_T} \frac{d\varphi_k}{dZ} \varphi_j \varphi_i dZ \\
 + \mu^2 \sum_{j=i-1}^{i+1} H_j^1 \int_{Z_0}^{Z_T} \varphi_j \varphi_i dZ .
 \end{aligned} \tag{B.3}$$

$$\begin{aligned}
 \sum_{j=i-1}^{i+1} \frac{dD_j^2}{dt} \int_{Z_0}^{Z_T} \varphi_j \varphi_i dZ &= \int \sum_{j=i-1}^{i+1} A_j^2 \int_{Z_0}^{Z_T} \varphi_j \varphi_i dZ \\
 + \mu \sum_{k=i-1}^{i+1} \bar{u}^k \sum_{j=i-1}^{i+1} D_j^1 \int_{Z_0}^{Z_T} \varphi_j \varphi_k \varphi_i dZ \\
 - \beta \sum_{j=i-1}^{i+1} U_j^2 \int_{Z_0}^{Z_T} \varphi_j \varphi_i dZ . \\
 - \mu \sum_{k=i-1}^{i+1} \bar{u}^k \sum_{j=i-1}^{i+1} W_j^1 \int_{Z_0}^{Z_T} \frac{d\varphi_k}{dZ} \varphi_j \varphi_i dZ \\
 + \mu^2 \sum_{j=i-1}^{i+1} H_j^2 \int_{Z_0}^{Z_T} \varphi_j \varphi_i dZ .
 \end{aligned} \tag{B.4}$$

3. Thermodynamic Equations (2.29) and (2.30) :

$$\begin{aligned}
 & \sum_{j=i-1}^{i+1} \frac{dT_1^j}{dt} \int_{Z_0}^{Z_T} \varphi_j \varphi_i dZ = \\
 & - \mu \sum_{k=i-1}^{i+1} \bar{u}^k \sum_{j=i-1}^{i+1} T_2^j \int_{Z_0}^{Z_T} \varphi_j \varphi_k \varphi_i dZ \\
 & + \frac{f}{R} \sum_{k=i-1}^{i+1} \bar{u}^k \sum_{j=i-1}^{i+1} v_{j1} \int_{Z_0}^{Z_T} \frac{d\varphi_k}{dZ} \varphi_j \varphi_i dZ \\
 & - \sum_{k=i-1}^{i+1} \bar{T}^k \sum_{j=i-1}^{i+1} w_{j1} \int_{Z_0}^{Z_T} \frac{d\varphi_k}{dZ} \varphi_j \varphi_i dZ \\
 & + \sum_{j=i-1}^{i+1} Q_{j1} \int_{Z_0}^{Z_T} \varphi_j \varphi_i dZ .
 \end{aligned} \tag{B.5}$$

$$\begin{aligned}
 & \sum_{j=i-1}^{i+1} \frac{dT_2^j}{dt} \int_{Z_0}^{Z_T} \varphi_j \varphi_i dZ = \\
 & + \mu \sum_{k=i-1}^{i+1} \bar{u}^k \sum_{j=i-1}^{i+1} T_1^j \int_{Z_0}^{Z_T} \varphi_j \varphi_k \varphi_i dZ \\
 & + \frac{f}{R} \sum_{k=i-1}^{i+1} \bar{u}^k \sum_{j=i-1}^{i+1} v_{j2} \int_{Z_0}^{Z_T} \frac{d\varphi_k}{dZ} \varphi_j \varphi_i dZ \\
 & - \sum_{k=i-1}^{i+1} \bar{T}^k \sum_{j=i-1}^{i+1} w_{j2} \int_{Z_0}^{Z_T} \frac{d\varphi_k}{dZ} \varphi_j \varphi_i dZ \\
 & + \sum_{j=i-1}^{i+1} Q_{j2} \int_{Z_0}^{Z_T} \varphi_j \varphi_i dZ .
 \end{aligned} \tag{B.6}$$

APPENDIX C

BASIS FUNCTION EQUATIONS FOR FEM-A

1. Notation:

$$\begin{aligned}\Delta_i &= Z_i - Z_{i-1} \\ \Delta'_i &= Z'_i - Z'_{i-1} \\ \xi &= Z - Z_i\end{aligned}$$

2. For the general case:

$$\begin{aligned}\varphi_i(\xi) &= \frac{\xi - \Delta'_i + .5\Delta'_{i-1}}{.5(\Delta'_i + \Delta'_{i-1})} & -\Delta'_2 - \frac{\Delta'_{i-1}}{2} \leq \xi \leq -\frac{\Delta'_i}{2} \\ &= \frac{-\xi + .5\Delta'_{i+1}}{.5(\Delta'_i + \Delta'_{i+1})} & -\frac{\Delta'_i}{2} \leq \xi \leq \frac{\Delta'_{i+1}}{2}\end{aligned}$$

for any i sufficiently far from the boundaries, $3 \leq i \leq n$.

$$\begin{aligned}\psi_i(\xi) &= \frac{\xi + \Delta'_i}{\Delta_i} & -\Delta'_i \leq \xi \leq 0 \\ &= \frac{-\xi + \Delta'_{i+1}}{\Delta'_{i+1}} & 0 \leq \xi \leq \Delta'_{i+1}\end{aligned}$$

for $2 \leq i \leq n$.

3. For special cases, $\varphi_1, \varphi_2, \varphi_{n+1}, \varphi_{n+2}, \psi_1, \psi_{n+1}$

$$\varphi_1(\xi) = \frac{-\xi + .5\Delta'_2}{\Delta'_2}$$

$$\varphi_2(\xi) = \frac{\xi + 1.5\Delta'_2}{\Delta'_2} \quad -\Delta'_2 \leq \xi \leq -.5\Delta'_2$$

$$= \frac{-\xi + .5\Delta'_3}{.5(\Delta'_2 + \Delta'_3)} \quad -.5\Delta'_2 \leq \xi \leq .5\Delta'_3$$

$$\psi_1(\xi) = \frac{-\xi + \Delta'_2}{\Delta'_2} \quad 0 \leq \xi \leq \Delta'_2$$

$$\psi_{n+1}(\xi) = \frac{\xi + \Delta'_{n+1}}{\Delta'_{n+1}}$$

$$\varphi_{n+1}(\xi) = \frac{\xi + \Delta'_{n+1} + .5\Delta'_n}{.5(\Delta'_{n+1} + \Delta'_n)} \quad -\frac{\Delta'_n}{2} - \Delta'_{n+1} \leq \xi \leq -\frac{\Delta'_{n+1}}{2}$$

$$= \frac{-\xi + .5\Delta'_{n+1}}{\Delta'_{n+1}} \quad 0 \leq \xi \leq -\Delta'_{n+1}$$

$$\varphi_{n+2}(\xi) = \frac{\xi + .5\Delta'_{n+1}}{\Delta'_{n+1}}$$

APPENDIX D

GALERKIN FORM OF FEM-B PROGNOSTIC EQUATIONS

1. The vorticity equations have the same form as the vorticity equations for model FEM-A, equations (B.1) and (B.2).
2. The divergence equations are the same as the divergence equations in model FEM-A, equations (B.3) and (B.4).
3. Thermodynamic Equations (2.29) and (2.30) :

$$\begin{aligned}
 & \sum_{j=i-1}^{i+1} \frac{dT_j}{dt} \int_{Z_0}^{Z_T} \psi_j \psi_i dZ = \\
 & - \mu \sum_{k=i-1}^{i+1} \bar{u}^k \sum_{j=i-1}^{i+1} T_j^2 \int_{Z_0}^{Z_T} \psi_j \phi_k \psi_i dZ \\
 & + \frac{f}{R} \sum_{k=i-1}^{i+1} \bar{u}^k \sum_{j=i-1}^{i+1} v_j^1 \int_{Z_0}^{Z_T} \frac{d\phi_k}{dZ} \phi_j \psi_i dZ \\
 & - \sum_{k=i-1}^{i+1} \bar{T}^k \sum_{j=i-1}^{i+1} w_j^1 \int_{Z_0}^{Z_T} \frac{d\psi_k}{dZ} \psi_j \psi_i dZ \\
 & + \sum_{j=i-1}^{i+1} Q_j^1 \int_{Z_0}^{Z_T} \psi_j \psi_i dZ .
 \end{aligned} \tag{D.1}$$

$$\begin{aligned}
& \sum_{j=i-1}^{i+1} \frac{dT_j^2}{dt} \int_{Z_0}^{Z_T} \psi_j \psi_i dZ = \\
& + \mu \sum_{k=i-1}^{i+1} \bar{u}^k \sum_{j=i-1}^{i+1} T_j^1 \int_{Z_0}^{Z_T} \psi_j \phi_k \psi_i dZ \\
& + \frac{f}{R} \sum_{k=i-1}^{i+1} \bar{u}^k \sum_{j=i-1}^{i+1} V_j^2 \int_{Z_0}^{Z_T} \frac{d\phi_k}{dZ} \phi_j \psi_i dZ \\
& - \sum_{k=i-1}^{i+1} \bar{T}^k \sum_{j=i-1}^{i+1} W_j^1 \int_{Z_0}^{Z_T} \frac{d\psi_k}{dZ} \psi_j \psi_i dZ \\
& + \sum_{j=i-1}^{i+1} Q_j^2 \int_{Z_0}^{Z_T} \psi_j \psi_i dZ .
\end{aligned} \tag{D.2}$$

Note that in these equations the basis functions are functions of Z ($\phi_i = \phi_i(Z)$ and $\psi_i = \psi_i(Z)$). All of the other variables, Q , T , u , V , and W , are functions of time ($Q_i = Q_i(t)$, $T_i = T_i(t)$, $u = u(t)$, $V_i = V_i(t)$, $W_i = W_i(t)$).

APPENDIX E FORCED VERTICAL VELOCITY

1. The contribution to the surface geopotential from the forced vertical velocity is ϕ_s .

$$\begin{aligned}\phi_s(x,t) &= \phi_m \sin^2(\pi t/2T) \sin(\mu x) & t \leq T \\ &= \phi_m \sin(\mu x) & t > T,\end{aligned}\quad (E.1)$$

where ϕ_m is mountain geopotential (m^2/s^2), t is time, and T is the total time to build the mountain. ϕ_m is a constant,

$$\phi_m = gH_m, \quad (E.2)$$

where g is gravity and H_m is the height of the mountain. H_m is a parameter specified in each model. $H_m = 750$ meters in the thesis experiments.

2. The time rate of change of ϕ_s is separated into sine and cosine components for use in the surface geopotential forecast equations,

$$\frac{d\phi_s}{dt} = MTS_1(t) \cos(\mu x) + MTS_2(t) \sin(\mu x), \quad (E.3)$$

$$\text{where } \frac{d}{dt} = \frac{\partial}{\partial t} + \bar{u}_{sfc} \frac{\partial}{\partial x}.$$

Equation (E.1) is substituted into equation (E.3) and the resultant expression is separated into sine and cosine equations. The equations to calculate the terms MTS_1 and MTS_2 are

$$\begin{aligned}MTS_1(t) &= \bar{u}_{sfc} \phi_m \mu \sin^2(\pi t/2T) & t \leq T \\ &= \bar{u}_{sfc} \phi_m \mu & t > T,\end{aligned}\quad (E.4)$$

and

$$\begin{aligned}
 \text{MTS}_2(t) &= \frac{\pi \phi_m}{T} \sin(\pi t/2T) \cos(\pi t/2T) & t \leq T \\
 &= 0 & t > T.
 \end{aligned}
 \tag{E.5}$$

These terms are calculated for each time step in the model's forecast subroutine.

APPENDIX F

DIABATIC HEATING TERMS

For the diabatic heating function defined in equation (3.1), the maximum heating occurs at $Z = 0.50$, the midpoint of the heated layer. Temperature and diabatic heating are defined at the staggered levels for grid A, and at the unstaggered levels for grid B. Consequently, the rate of heating differs between the staggered and unstaggered models. In these experiments, the heated layer is between $Z = 0.40$ and $Z = 0.60$, the heating rate is 5.0 K/day , and only the cosine term, Q_1 , is nonzero in the heated layer. The value of the heating term is listed below for staggered and unstaggered levels for six-, twelve- and sixty-layer models.

Grid A Six-Layer Models

Z	Q_1
0.250	0.000000E+00
0.417	0.387657E-05
0.583	0.387668E-05
0.750	0.000000E+00

Grid B Six-Layer Models

Z	Q_1
0.333	0.000000E+00
0.500	0.578704E-04
0.667	0.000000E+00

Grid A Twelve-Layer Models

Z	Q_1
0.375	0.000000E+00
0.458	0.364241E-04
0.542	0.364243E-04
0.625	0.000000E+00

Grid B Twelve-Layer Models

Z	Q_1
0.333	0.000000E+00
0.417	0.387657E-05
0.500	0.578704E-04
0.583	0.387668E-05
0.667	0.000000E+00

Grid A Sixty-Layer Models

Z	Q_1
0.392	0.000000E+00
0.408	0.985885E-06
0.425	0.847474E-05
0.442	0.214459E-04
0.458	0.364238E-04
0.475	0.493952E-04

Grid B Sixty-Layer Models

Z	Q_1
0.400	0.000000E+00
0.417	0.387660E-05
0.433	0.144676E-04
0.450	0.289351E-04
0.467	0.434028E-04
0.483	0.539938E-04

0.492	0.568843E-04	0.500	0.578704E-04
0.508	0.568845E-04	0.517	0.539938E-04
0.525	0.493957E-04	0.533	0.434028E-04
0.542	0.364246E-04	0.550	0.289352E-04
0.558	0.214466E-04	0.567	0.144677E-04
0.575	0.847529E-05	0.583	0.387665E-05
0.592	0.986071E-06	0.600	0.929893E-16
0.608	0.000000E + 00	0.617	0.000000E + 00

LIST OF REFERENCES

- Arakawa, A., 1984: Vertical differencing of filtered models. *Proc. of European Centre for Medium Range Weather Forecasts: 1983 Seminar on Numerical Method for Weather Prediction*, 1, 183-206.
- , and V. R. Lamb, 1977: Computational design of the basic dynamical processes of the UCLA general circulation model. *Methods of Computational Physics*, 17, 173-265.
- Charney, J. G., and N. A. Phillips, 1953: Numerical integration of the quasigeostrophic equations for barotropic and simple baroclinic flows. *J. of Meteor.*, 10, 71-79.
- Cullen, M. J. P., 1973: A simple finite-element method for meteorological problems. *J. Inst. Math Applies.*, 11, 15-31.
- Gall, R. L., 1976: A comparison of linear baroclinic theory with the eddy statistics of a general circulation model. *J. Atmos. Sci.*, 33, 349-373.
- Gray, W. G., and G. F. Pinder, 1976: An analysis of the numerical solution of the transport equation. *Water Resour. Res.*, 12, 547.
- Haltiner, G. J., and R. T. Williams, 1980: *Numerical Prediction and Dynamic Meteorology*. John Wiley and Sons, Inc., 477 pp.
- Hinsman, D. E., 1975: Application of a finite element method to the barotropic primitive equations. M. S. Thesis, Naval Postgraduate School, Monterey, CA 93943, 116 pp.
- Hoskins, B. J., and F. Bretherton, 1972: Atmospheric frontogenesis models: Mathematical formulation and solution. *J. Atmos. Sci.*, 29, 11-37.
- Jordan, M. S., 1985: A comparison of six vertical discretization schemes. M. S. Thesis, Naval Postgraduate School, Monterey, CA 93943, 174 pp.
- Lorenz, E. N., 1960: Energy and numerical weather prediction. *Tellus*, 12, 364-373.
- Neta, B., and R. T. Williams, 1986: Stability and phase speed for various finite element formulations of the advection equation. *Computers and Fluids*, 14, 393-410.
- , ———, and D. E. Hinsman, 1986: Studies in a shallow water fluid model with topography, in *Numerical Mathematics and Applications* (R. Vichevetsky, J. Vignes, eds.). *Elsevier Sci. Pub.*, 347-354.
- Schoenstadt, A. L., 1980: A transfer function analysis of numerical schemes used to simulate geostrophic adjustment. *Mo. Wea. Rev.*, 108, 1245-1259.

Staniforth, A. N., and R. W. Daley, 1977: A finite-element formulation for the vertical discretization of sigma-coordinate primitive equation models. *Mo. Wea. Rev.*, **105**, 1108-1118.

———, ———, 1979: A baroclinic finite-element model for regional forecasting with the primitive equations. *Mo. Wea. Rev.*, **107**, 107-121.

Staniforth, A. N., and H. L. Mitchell, 1977: A semi-implicit finite-element barotropic model. *Mo. Wea. Rev.*, **106**, 439-447.

———, ———, 1978: A variable-resolution finite-element technique for regional forecasting with the primitive equations. *Mo. Wea. Rev.*, **106**, 439-447.

Tokioka, T., 1978: Some considerations on vertical differencing. *J. of the Met. Soc. of Japan*, **56**, 98-111.

Williams, R. T., 1967: Atmospheric frontogenesis: A numerical experiment. *J. Atmos. Sci.*, **24**, 627-641.

Winninghoff, F., 1968: On the adjustment toward a geostrophic balance in a simple primitive equation model with application to the problem on initialization and objective analysis. Doctoral dissertation, UCLA.

Zienkiewicz, O. C., 1977: *The Finite Element Method*. McGraw-Hill, New York, 787 pp.

INITIAL DISTRIBUTION LIST

	No. Copies
1. Defense Technical Information Center Cameron Station Alexandria, VA 22304-6145	2
2. Library, Code 0142 Naval Postgraduate School Monterey, CA 93943-5002	2
3. Meteorology Reference Center, (Code 63) Department of Meteorology Naval Postgraduate School Monterey, CA 93943-5000	1
4. Chairman (Code 63Rd) Department of Meteorology Naval Postgraduate School Monterey, CA 93943-5000	1
5. Dr. Roger T. Williams, (Code 63Wu) Department of Meteorology Naval Postgraduate School Monterey, CA 93943-5000	5
6. Professor B. Neta (Code 53Nd) Department of Mathematics Naval Postgraduate School Monterey, CA 93943-5000	5
7. USAF ETAC/LD Air Weather Service Technical Library Scott AFB, IL 62225-5000	1
8. Program Manager (AFIT/CIR) Air Force Institute of Technology Wright-Patterson AFB, OH 45433	1
9. Commander Air Weather Service Scott AFB, IL 62225	1
10. Commander Air Force Global Weather Central Offutt AFB, NE 68113	1
11. Commander Naval Oceanography Command NSTL Station	1

- Bay St. Louis, MS 39522
12. Chief of Naval Research 1
800 N. Quincy Street
Arlington, VA 22217
 13. Commanding Officer 1
Naval Environmental Prediction Research Facility
Monterey, CA 93943-5000
 14. Commanding Officer 1
Fleet Numerical Oceanography Center
Monterey, CA 93943-5000
 15. Commanding Officer 1
Naval Ocean Research and Development Activity
NSTL Station
Bay St. Louis, MO 39522
 16. D. Morris Shapiro 2
937 West 1820 South
Salt Lake City, UT 84104
 17. Lt. Bruce G. Shapiro, USAF 4
General Delivery
Box 99999
Offutt AFB, NE 86113
 18. Captain Mary S. Jordan, USAF 1
Det 11, 2d Weather Squadron
Patrick Air Force Base, FL 32925
 19. Professor R. L. Elsberry (Code 63Es) 1
Department of Meteorology
Naval Postgraduate School
Monterey, CA 93943-5000
 20. Professor R. L. Haney (Code Hy) 1
Department of Meteorology
Naval Postgraduate School
Monterey, CA 93943-5000
 21. Professor A. L. Schoenstadt (Code 53Zh) 1
Department of Mathematics
Naval Postgraduate School
Monterey, CA 93943-5000
 22. Professor R. E. Newton (Code 69Ne) 1
Department of Mechanical Engineering
Naval Postgraduate School
Monterey, CA 93943-5000
 23. Professor M. A. Rennick (Code 63Rn) 1
Department of Meteorology
Naval Postgraduate School

Monterey, CA 93943-5000

- | | | |
|-----|---------------------------------------------------------------------------------------------------------------------------------------------------------------|---|
| 24. | Dr. J. Steppeler
European Center for Medium Range Weather Forecasts
Shinfield Park
Reading, Berkshire RG2 9AX
England | 1 |
| 25. | CDR Donald E. Hinsman, USN
Assistant for Environmental Science
Room 5E813 OASN (RE and S)
Pentagon
Washington, D. C. 20350-1000 | 1 |
| 26. | Dr. Eugene S. Takle
Department of Climatology and Meteorology
310 Curtiss Hall
Iowa State University
Ames, IA 50011 | 1 |
| 27. | Dr. M.J.P. Cullen
Meteorological Office
Bracknell, Berks, United Kingdom | 1 |
| 28. | Dr. Robert L. Lee
Atmospheric and Geophysical Science Division
University of California
P.O. Box 808
Livermore, CA 94550 | 1 |
| 29. | Dr. N. A. Phillips
National Meteorological Center/NOAA
World Weather Building
Washington, D.C. 20233 | 1 |
| 30. | Dr. Y. Sasake
Department of Meteorology
University of Oklahoma
Norman, OK 73069 | 1 |
| 31. | Dr. Andrew Staniforth
Recherche-en-Prevision Numerique
West Isle Office Tower, 5 ieme itage
2121 route Trans-Canada
Dorval, Quebec H9P1J3, Canada | 1 |
| 32. | Professor O. C. Zienkiewicz
Head of Civil Engineering Department
Applied Science Building
Singleton Park
Swansea SA2 8PP
United Kingdom | 1 |

END

DATE

FILM

JAN
1988